DIAGNOSTICS

M. Minty
Deutsches Elektronen Synchrotron (DESY), Hamburg, Germany

Abstract
The beam diagnostics considered here concentrate on those with most frequent application in synchrotron radiation and free electron laser facilities. Focus is placed on the description of the experimental hardware in the immediate vicinity of the beam. We describe the various instruments used for determining the most easily measured moments of the beam distribution, namely, the beam charge, the beam positions, the transverse and longitudinal beam sizes, and the bunch energy spread. Common algorithms for determining the transverse beam emittances are also outlined.

1. INTRODUCTION

Optimum accelerator performance depends critically on the ability to carefully measure and control the properties of the particle beams. As the demands for higher beam currents, smaller beam emittances, and tighter tolerances on the beam parameters have increased in recent years, the types of problems encountered in practice have evolved and the diagnostics used to characterize the beams have correspondingly been improved and refined.

The rapid evolution of developments in beam instrumentation has resulted in numerous published reports, only a portion of which are cited here. A selection of classic references, from which I have greatly profited, include "Diagnostics" by J. Borer and R. Jung [1], a comprehensive report including signal processing techniques and schematics and photographs of many detectors used at CERN; "Beam Instrumentation" by R. Littauer [2]; "Beam Diagnostics and Applications by A. Hofmann [3], which details many high-level applications using beam diagnostics; and "Bunched Beam Diagnostics" [4] and "Spectral Analysis of Relativistic bunched Beams" [5] by R.H. Siemann, which provide an excellent introduction to frequency domain analysis including application to the study of beam instabilities. More recently, several excellent tutorials in beam diagnostics have been published in the proceedings of the beam instrumentation workshops (BIW) and in the invited talks of the diagnostics conferences (DIPAC).

For the purpose of these lectures, we consider beam diagnostics to consist of:

i) the measurement device (the focus of this lecture);

ii) the associated electronics and processing hardware (the subject of numerous publications and internal reports, which are often application specific);

iii) high-level applications (for example by A. Hofmann [3]).

Personally I find the topic of beam diagnostics and their applications to be not only extremely interesting per se (i.e. studying limits on the ultimately achievable resolution of a particular measurement diagnostic), but also, on a day-to-day basis, relevant for defining, diagnosing, and solving problems related to the control of particle beams. It has often been my experience that the design of a good experiment and the interpretation and analysis of the experimental data demand a thorough understanding of the measurement device itself. As an example, suppose ion-related phenomena are suspected to be the cause of observed emittance growth or beam

instability. For diagnosis, one might consider using beam position monitor electrodes as clearing electrodes. To do so these questions might be relevant: "what kind of beam position monitors can be appropriately biased to clear the suspected ions?" or (in the study of beam instabilities) "what should the frequency spectra look like *without* instabilities". To address these questions, an understanding of the diagnostics themselves is often required.

In these lectures we describe the hardware used for measurements of the beam charge and intensity (section 3) and the beam position (section 4). Methods for determining the transverse beam emittance are described together with the apparatus used for the required measurements of the transverse beam size (section 5). Techniques are also presented for measurements of the beam energy spread (section 6) and the bunch length (section 7). A summary is given in section 8. The presented methods focus on applications in linac-based free electron lasers and synchrotron radiation facilities. Examples of beam diagnostics measurements from existing facilities are given throughout the text.

2. DETECTOR SENSITIVITY

The electric field of a relativitic particle in a smooth vacuum chamber is depicted in Fig. 1. The field lines are relativistically contracted into a "Lorentz-contracted pancake". These induce a wall current $i_w(t)$ which has opposite sign of the beam current $i_b(t)$: $i_b(t)=-i_w(t)$.

From the point of view of a beam detector, which detects properties of the charged particle beam, the wall current may be viewed as a current source. With infinite output impedance, the wall current i_w will therefore flow through any impedance placed in its path. Many "classical" beam detectors consist of a modification of the walls through which the currents will flow.

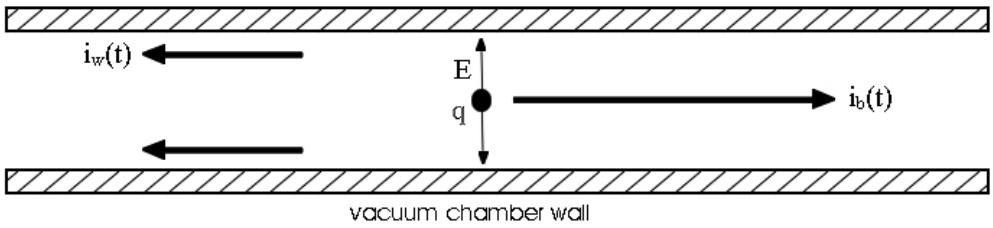

Fig. 1 Beam (i_b) and wall (i_w) current induced by the electric field E of the bunch of charge q.

In the following, we will refer to the sensitivity S(ω) of the detector. For measurement of the beam charge,

$$S(\omega) = \frac{V(\omega)}{I_w(\omega)} \tag{1}$$

(in units of Ω) which is the ratio of the signal size developed V(ω) to the wall current $I_w(\omega)$. For measurement of the beam position,

$$S(\omega) = \frac{V(\omega)}{D(\omega)} \tag{2}$$

(in units of Ω/m) which is the ratio of the signal size developed to the dipole mode of the distribution, given by D(ω)=I(ω)z, with z=x,y in the horizontal (x) and vertical (y) plane respectively.

3. BEAM CHARGE AND INTENSITY

3.1 Beam Charge – the Faraday Cup

Measurements of the beam charge using a Faraday cup [6-8] are usually invasive and typically used only at low beam energies (up to a few hundred MeV). In such applications, the cup is inserted directly into the path of the beam which may consist of a single bunch or of a train of bunches. Compared to other types of beam charge monitors, the calibration of the Faraday Cup does not depend on the time structure of the beam.

A conceptual view of a Faraday cup is shown in Fig. 2. The cup itself consists of a thick or series of thick conducting materials (e.g. Cu, C, Pb. Ta) of sufficient area to fully intercept the beam. The constituency and thickness L of the intercepting material, which are chosen depending on the beam energy E, is such that the energy of the particles in the beam is completely absorbed: E=(dE/dx)L, where the energy loss per unit length dE/dx depends on the absorber material [9]. For example, ~0.4 m of copper is sufficient to stop 1 GeV electrons. The beam charge is converted into a corresponding current. The voltage V measured across a resistor R to ground provides a measure of the instantaneous current absorbed. In practice, a direct current (dc) bias is often applied to the cup to retain the electrons produced by secondary emission. Impedance matching is essential and termination is usually made into 50Ω. The detector is typically bandwidth limited to ~1 GHz due to the capacitance to ground.

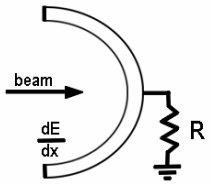

Fig. 2 Conceptual view of a Faraday cup.

Shown in Fig. 3 is a schematic of the Faraday cup used in the injector linac for KEKB [10,11]. The cylindrically symmetric structure contains lead, iron, and carbon blocks. In this application, the thickness of the lead block corresponds to about 35 radiation lengths so that the beams are fully absorbed by the block. The carbon and ion blocks serve to suppress electromagnetic showers generated in the lead block. The bias voltage (several hundred Volts) is supplied to suppress both secondary emission from the target material and secondary electrons generated in the residual gas of the vacuum environment.

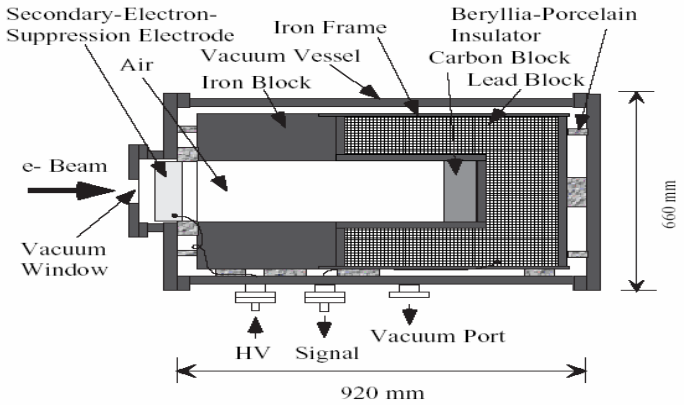

Fig. 3 Schematic of the Faraday cup used for in the KEKB injector linac (courtesy T. Suwada, 2003).

3.2 Beam Intensity - Toroids

The choice of design of transformers for measuring the beam intensity using toroids reflects the time structure of the beam. For beams with no time-dependent structure (true dc beams), second harmonic detectors, also refered to as direct-current current transformers are used[1]. In storage rings or in linear accelerators with pulsed beam currents, conventional current transformers are used, usually to obtain the dc-component (i.e. total charge) of the beam. In FEL linacs and light sources with multiple closely spaced bunches, integrating current transformers are often used to measure the single-bunch charge. In the latter two cases, these magnetic detectors sense the change in the magnetic flux caused by the electromotive force (emf) induced in response to the beam's azimuthal magnetic field.

Consider a magnetic ring (e.g. ferrite, iron, or a tape-wound core) surrounding the beam, as shown in Fig. 4a. From Ampere's law,

$$\oint \vec{B} \cdot \vec{dl} = \mu I \tag{3}$$

where the integration over the field B and length element dl is taken over the magnetic path length (e.g. the circumferential length of the magnetic core), μ is the permeability of the core ($=\mu_r\mu_0$, where μ_r is the magnetic permeability of the medium and $\mu_0=4\pi\times 10^{-7}$ [H/m] is the permeability of free space), and I is the intercepting beam current. If the radius r_0 is much greater than the thickness of the toroid (as is typical by design) and if the beam is centered in the toroid, then the field B may be approximated by the average value of the field in the magnetic core $\langle B_n \rangle$ and is given by

$$B = \langle B_n \rangle = \frac{\mu i_b}{2\pi r_0} \tag{4}$$

Here the subscript n denotes the component of the magnetic field normal to the cross sectional area the core. The induced electromotive voltage ε, is related to the magnetic flux ϕ through a cross-sectional area element of the coil da by

$$\begin{aligned} \epsilon &= \frac{d\phi}{dt} \text{ where } \phi = \int \vec{B} \cdot d\vec{a} \\ &= \frac{\mu A}{2\pi r_0}\frac{di_b}{dt} \end{aligned} \tag{5}$$

where A is the cross-sectional area of the magnetic ring. If now an N-turn coil is additionally wound around the core, as depicted in Fig. 4b, this coil senses the induced electromotive force (emf), which acts to oppose the magnetic field induce by the beam. In the classical sense, the N-turn coil serves as a primary/secondary winding of a current transformer while the intercepting beam acts as a secondary/primary winding, respectively. By loading the circuit with an series impedance R, the observed voltage across the resistor is by Lenz's law, a scaled (by the turns ratio N) replica of the beam current: $V_r=I_rR=(I_b/N)R$.

The bandwidth characteristics, not taking into account limitations from the processing electronics, are determined by the inductance L which is given by $L=N^2/R_h$, where the reluctance

[1] The phrase DCCT is also used particularly by the storage ring community to describe bunched beam current transformers which detect the DC component (total current) of the stored beam.

of the magnetic path is $R_h=l/\mu\cdot A$ in H^{-1} and l is the length of the magnetic path (i.e. the mean circumference of the toroid). Then

$$L = \frac{N^2 \mu_r \mu_0 A}{l} \tag{6}$$

Modeled as an idealized parallel R-L circuit, the sensitivity is

$$S = \frac{R}{\sqrt{1+(\frac{\omega_l}{\omega})^2}} \tag{7}$$

where the low frequency cutoff ω_l is $\omega_l=R/L$.

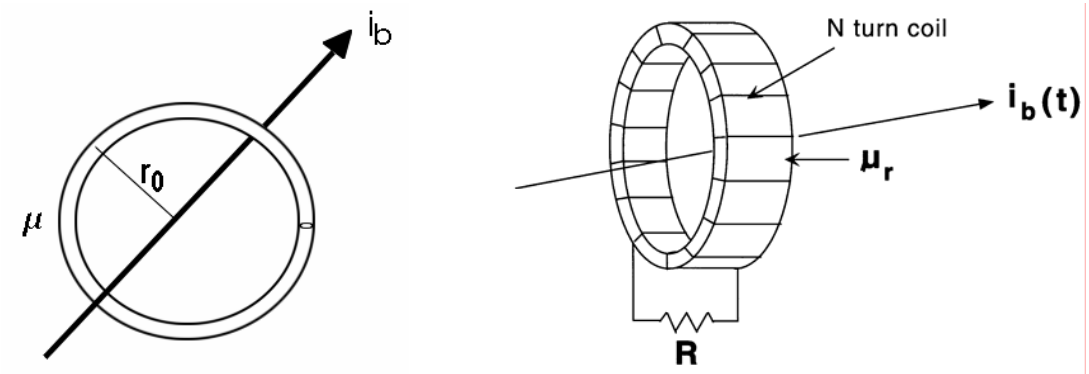

Fig. 4 Conceptual sketches of a beam current transformer for which the beam acts as a primary winding (left) while an N-turn coil serves as the secondary winding (right).

When a measure of the total beam current of interest, the cutoff frequency should be small. This may be achieved by making $L\sim N^2$ large or R small. However, the voltage across the resistor is

$$V(t) = \frac{i_b R}{N} e^{-(\frac{R}{L})t} \tag{8}$$

so that the detected voltage is small if N is large or R is small. Therefore a trade-off between bandwidth and signal amplitude must be made.

For detection of single-bunch beam currents, if the bunch spacing is small compared to the response time of the electronics, so-called "pile-up" effects (for which the detected signal amplitude does not decay to zero between bunches) may introduce systematic offsets. To minimize the effect of such distortions, care is taken to increase the high frequency cutoff, which arises ultimately from the stray capacitance of the windings.

A photograph of a commercially available current transformer is shown in Fig. 5. This beam charge monitor from Bergoz Precision Beam Instrumentation [12], which is based on K. Unser's design of a bunch-by-bunch monitor for LEP [13,14] at CERN, features the ability to detect single pulses in linacs or transfer lines with a resolution of 3×10^6 particles and in storage rings, a resolution of 10 nA for the circulating beam current.

Shown in Fig. 6 is a schematic of a toroidal transformer designed for beam intensity monitoring for use in the machine protection system at the TESLA test facility (TTF) at DESY [15]. For this application the total beam current (consisting of a train of pulses of up to 800 μs

total train length of maximum intensity of 8 mA with variable repetition frequency of up to 10 Hz) is of interest. By comparing the signals from two such detectors placed at different locations in the linac, any beam loss between the transformers could be detected and, if present, used to trigger the beam inhibit system.

Fig. 5 (One of many) current transformers available from Bergoz Precision Beam Instrumentation (courtesy J. Bergoz, 2003).

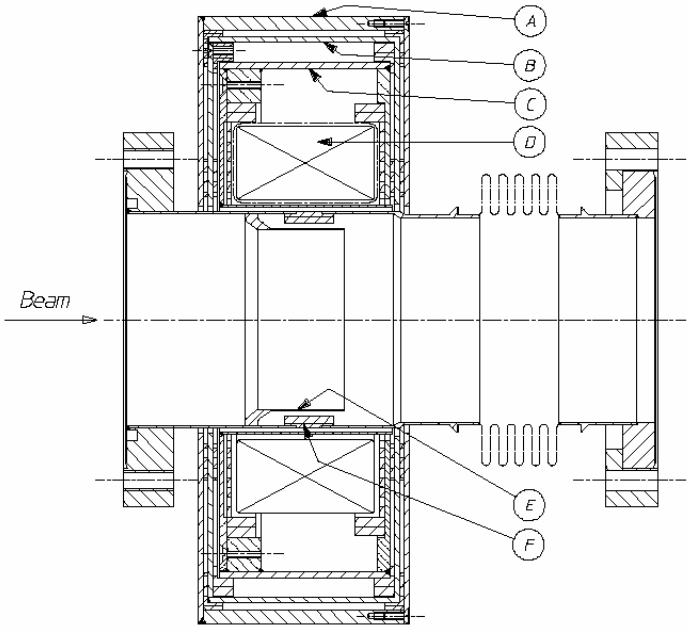

Fig. 6 Mechanical drawing of the toroidal transformer for use at the TESLA test facility showing iron (A), μ-metal (B), and copper (C) shields, the toroid itself (D) made from "Supermalloy", distributed by BF1 Electronique, France with $\mu=8\times10^4$, an electron shield (E), and a ceramic gap (F) (courtesy M. Jablonka, 2003).

Another example of a current transformer for the detection of single-bunch beam currents recently developed for use in the TTF at DESY is shown in Fig. 7. As can be seen in the photograph, the detector consists of 2 iron halves, which has the advantage that installation does not require opening the vacuum chamber. On the other hand, the low cutoff frequency is substantially increased due to the gaps between the two detector halves.

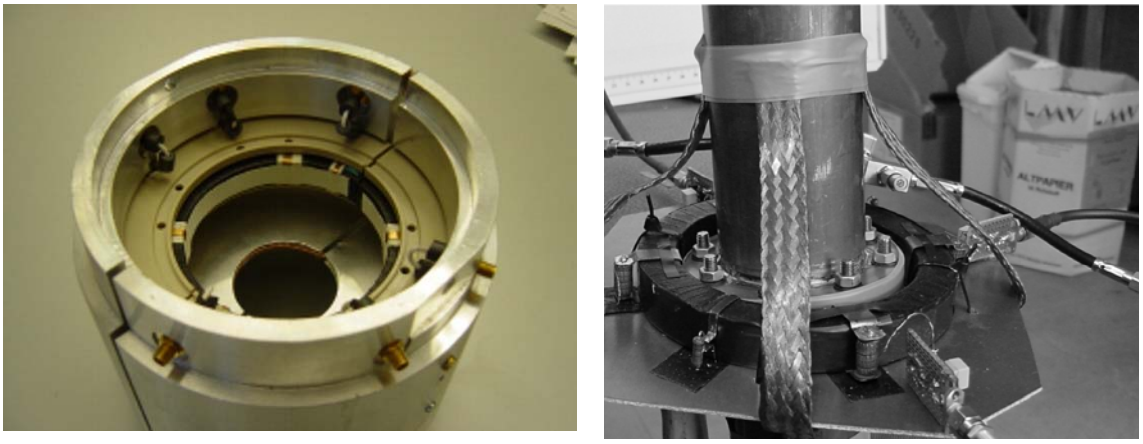

Fig. 7 Photograph of the fast toroid developed for the TESLA Test Facility (left) and measurement setup (right) showing the iron toroid, the 50 Ω effective output impedance, four bronze secondary windings, two additional calibration windings, and ferrite rings, which were added for suppression of a high frequency resonance (Courtesy D. Noelle, L. Schreiter, and M. Wendt, 2003).

4. BEAM POSITION MONITORS (BPMS)

Consider an array of "pickups" (to be described in detail in the next sections) placed symmetrically within the vacuum chamber. These may be used to measure both the total charge passing between them (the so-called "sum" signal) and the beam position (the "difference" signal). Due to the extra electronics required, BPM sum signals are not always available. However, the additional effort is especially worthwhile to allow for intensity-independent beam position information or, even without normalization, to localize beam losses in transport lines or at injection into a storage ring provided that the BPMs have single-turn readout capabilities.

A cross-sectional, conceptual view of a BPM is shown[2] in Fig. 8. The four pickups are label "U" for up, "D" for down, "L" for left, and "R" for right as seen from the point of view of the accelerated particles, for example. Denoting the induced voltage provided by each pickup by V, then for the geometry shown in Fig. 8, the relative beam positions are given by V_R-V_L in the horizontal plane (x) and V_U-V_D in the vertical plane (y). By "relative" is emphasized that the dipole moment (current times position) is measured. The beam intensity may be formed, for this example, by summing the voltages detected on two opposing pickups or by summing all pickups: V_R+V_L , V_u+V_D, or V_R+V_L +V_u+V_D. The intensity-independent beam position is given by normalizing the measured dipole moments to the measured beam intensity; for example, the horizontal position x is given by $x = V_R$-V_L / V_R+V_L. While elementary in principle, we will

[2] In e+/e- storage rings, the assembly is usually tilted by 45 degrees to avoid synchrotron radiation from striking the electrodes. Processing of the beam position information must take into account the modified geometry.

show that there are higher-order nonlinearities, depending on the pickup design, that must considered particularly in the case of non-perfectly steered (far off-axis) beams.

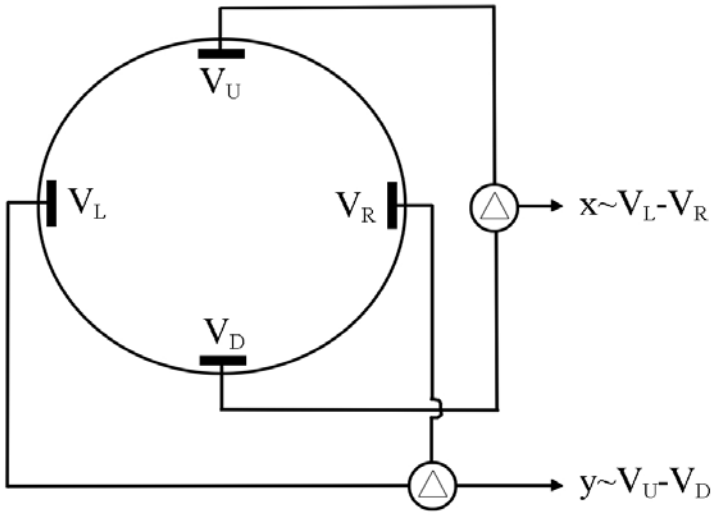

Fig. 8 Conceptual view of a beam position monitor used for detecting the horizontal (x) and vertical (y) beam positions.

4.1 Beam Position – Wall Gap Monitor (WGM)

Consider the simple geometry shown in Fig. 9. Here a portion of the vacuum chamber has been removed and replaced with some resistive material with effective impedance Z (representing the effective output impedance seen by the beam). When the bunch passes the detector, a wall current flows in the opposite direction. Detection of the voltage across the impedance then gives a direct measurement of the beam current since $V = i_w(t)Z = -i_b(t)Z$. In practice, the removed portion of the vacuum chamber is replaced with a nonconducting (for example, ceramic) material with resistors mounted across the gap to provide a path for the wall current. While simple in concept, this design is susceptible to environmental factors including electromagnetic pickup from pulsed devices (such as injection and extraction kickers and septa) and to ground loops (because the vacuum chamber is nominally grounded, not only does the wall current, but also power supply and/or vacuum pump return and leakage currents, for example, may flow directly through the resistors).

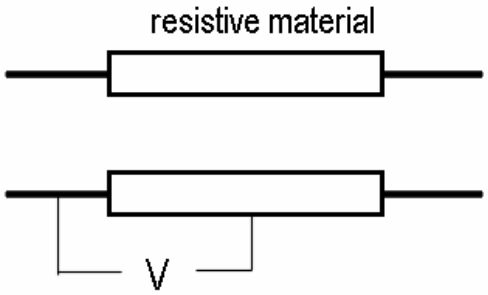

Fig. 9 Sketch of a simple wall gap monitor.

Typical refinements, as depicted in Fig. 10, include the addition of high permeability ferrite around the beam axis and a high-inductance metal enclosure (to protect from stray electromagnetic fields and to increase the impedance at high frequencies thus forcing the signal through the resistor), and perhaps multiple resistors (across which the voltage is to be measured) mounted usually in a cylindrically symmetric fashion. In the sketch of Fig. 10 (right), which shows an alternate topology, one of the resistors has been replaced by a coaxial line of equal impedance to be used for the signal processing. Such a device was used at CERN in the SPS accelerator [1] with eight 50 Ω resistors placed in parallel to form an equivalent impedance of 12.5 Ω.

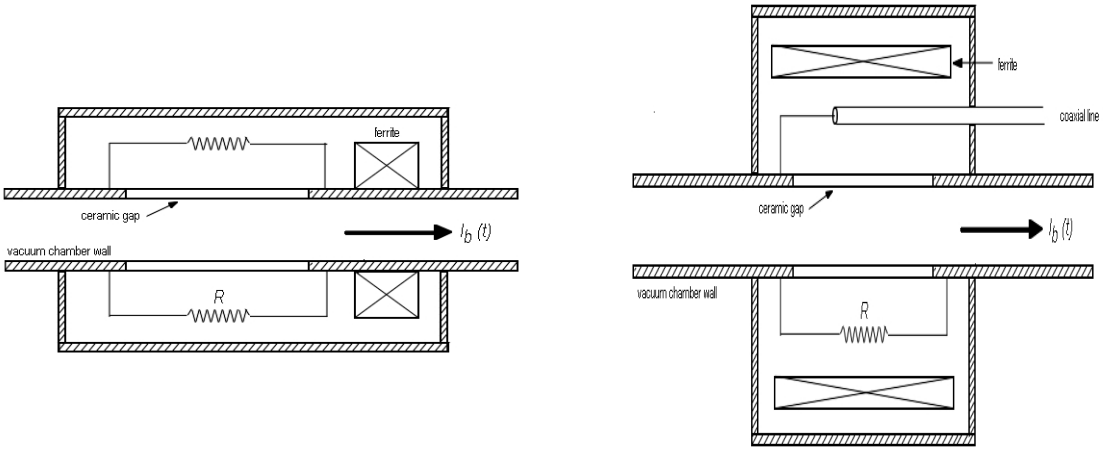

Fig. 10 Conceptual view of a wall gap monitor for two different geometries.

The sensitivity of the wall gap monitor, shown in Fig. 11, is considered from the idealized circuit model for the WGM consisting of a parallel RLC circuit with effective impedance Z:

$$\frac{1}{Z} = \frac{1}{R} + \frac{1}{j\omega L} + j\omega C \tag{9}$$

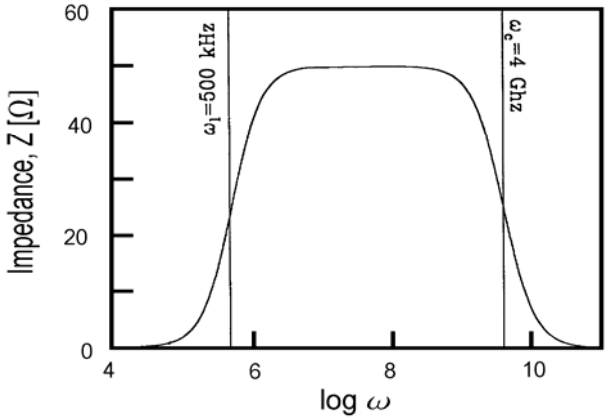

Fig. 11 Impedance of a resistive wall gap monitor with L=100 μH, C=5 pF, and R=40 Ω.

The high frequency response is determined by the capacitance C:

$$|Z(\omega \to \infty)| = \frac{R}{\sqrt{1+(\frac{\omega}{\omega_C})^2}} \quad \text{with} \qquad \omega_C = \frac{1}{RC} \tag{10}$$

while the low frequency response is determined by the inductance L:

$$|Z(\omega \to 0)| = \frac{R}{\sqrt{1+(\frac{\omega_L}{\omega})^2}} \qquad \text{with} \qquad \omega_L = \frac{R}{L} \tag{11}$$

In the intermediate regime, $R/L < \omega < 1/RC$. For high bandwidth therefore, L should be large while the resistance R and the capacitance C should be small. We remark that this simplified model does not take into account the fact that the shield may act as a resonant cavity (which is of importance for high-current storage rings in the context of impedances).

4.2 Beam Position – Electrostatic Monitors

Electrostatic monitors offer better immunity from environmental noise and may be used for detection of both the beam current and the beam position. These detectors consist of electrodes of length *l* upon which a voltage V is generated by the passing beam. A simple cylindrical capacitive monitor is shown in Fig. 12. The electrode is rigidly mounted and electrically isolated using insulating "standoffs". The vacuum chamber wall and the electrode act as a capacitor of capacitance C_e so the voltage generated on the electrode is $V=Q/C_e$ where $Q=i_w t=i_w l/c$ with c the speed of light in vacuum. The capacitive monitor can be represented by a series RC_e circuit. In the frequency domain, the detector sensitivity is constant in log ω for $\omega<\omega_C=1/RC_e$ and equal to R at higher frequencies.

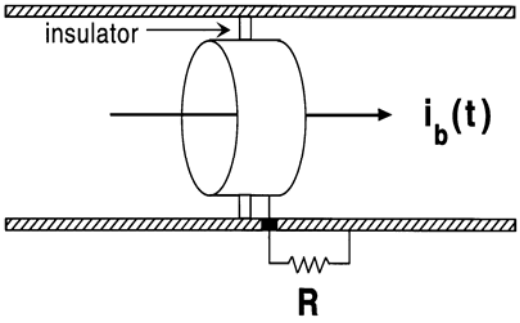

Fig. 12 Idealized sketch of a simple electrostatic monitor.

Since the capacitance C_e scales with electrode length *l*, then for fixed *l*, the output signal is determined by the input impedance R and the bunch length. For a pulse that is long ($\omega>\omega_C$) compared to the electrode length, the electrode becomes fully charged during the bunch passage. The output signal is therefore differentiated ($dV/dt=V/RC_e$). That is, the frequency response is limited by the detector bandwidth so the output pulse is broad and bipolar for frequencies $\omega<\omega_C$. In this case, the signal is often coupled out using a coaxial line attached to the electrode. The coupling impedance is $Z=1/C_e c$. For a coaxial line $C_e=lC$ and $Z_0=\text{sqrt}(L/C)$, where C and L are respectively the capacitance and inductance per unit length. Since $c=1/\text{sqrt}(LC)$, $Z_0=Z$ so, as expected, the impedance of the coaxial line should be made equal to the coupling impedance Z.

If the bunch length is short compared to the electrode length, then the induced voltage is usually directly detected through a high impedance amplifier. The impedance is chosen to be large so as to bleed the charge off the electrode. The output voltage rises rapidly and has amplitude proportional to the induced charge. This signal is followed by an extended negative tail (the dc component of the signal is zero). For very short bunches (less than about 1 cm), the signal may be bandwidth limited due to the processing of the signal. Typically high frequency cables (bandwidth ~20 GHz) are required and the signal should be viewed close to the source to minimize degradation of the signal due to the frequency-dependent attenuation in the cable.

In the following two examples, we consider, for simplicity, the case of termination into high output impedance so that the influence of geometrical considerations in detector design may be best illustrated.

4.2.1 Split-Plate Monitor

To obtain beam position information, the cylinder in Fig. 12 may be replaced by curved electrodes spanning an azimuth 2ψ. The azimuth is usually small to best suppress signal contributions from offsets in the plane not of interest. The detector is shown schematically in Fig. 13. The angle subtended by the electrodes is 2ψ and the electrodes have length *l*.

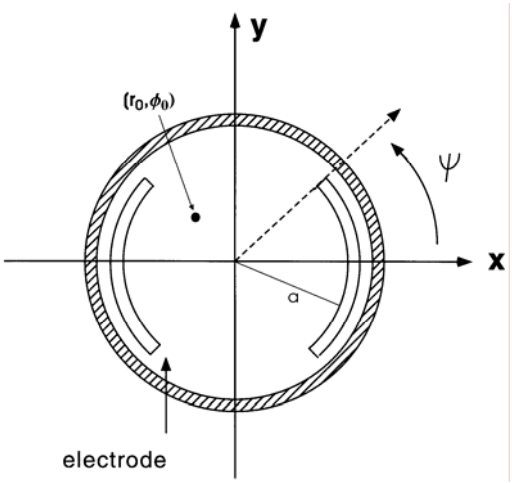

Fig. 13 Sketch of a split-plate capacitive monitor.

To determine the detector sensitivity, the induced voltage on each electrode must be determined. From Poisson's equation, using the polar coordinates (r and φ), the surface charge density σ due to a line charge λ collinear to the split plate at (r_0, φ_0) is

$$\sigma = \frac{\lambda}{2\pi a}[1 + \sum_{n=1}^{\infty}(\frac{r_o}{r})^2 \cos n(\phi - \phi_0)] \tag{12}$$

where a is the radial distance from the center of the monitor to the electrode. The current on each plate (I_L on the left and I_R on the right) is given by integrating the charge density over the entire area of the electrode:

$$\begin{aligned} I_R &= \int_{-\psi}^{+\psi} \sigma(r d\phi) \\ &= \frac{i_w}{2\pi}[2\psi + 2\frac{x_0}{a}\sin\psi + \frac{{x_0}^2 - {y_0}^2}{a^2}\sin 2\psi + ...] \end{aligned} \tag{13}$$

and

$$\begin{aligned} I_L &= \int_{\pi-\psi}^{\pi+\psi} \sigma(r\,d\phi) \\ &= \frac{i_w}{2\pi}[2\psi - 2\frac{x_0}{a}\sin\psi + \frac{{x_0}^2 - {y_0}^2}{a^2}\sin 2\psi + ...] \end{aligned} \tag{14}$$

The voltage or current on a single electrode depends on the detector geometry through the radius a, the length l, and the azimuthal angle subtended by the electrode 2ψ.

If, in the study of beam instabilities for example, the voltage of a single electrode is input into a frequency analyzer, higher harmonics (which have nothing to do with the nature of possible beam instabilities) will arise due to the nonlinearities inherent in this detector design.

Taking the difference of the currents times the impedance R gives the voltage to second order in the displacement x_0 and y_0

$$\begin{aligned} V &= (I_R - I_L)R \\ &= \frac{2i_w R}{\pi a}(\sin\psi)x_0 + ... \end{aligned} \tag{15}$$

and the sensitivity S, to second order, is

$$S = \frac{V}{i_w x_0} = \frac{2R}{\pi a}\sin\psi + ... \tag{16}$$

which is large if the azimuthal coverage is large or the radius is small. For example, with 2ψ=25º, R=50 Ω, and a=2.5 cm, the maximum sensitivity is about 0.5 Ω/mm.

4.2.2 Split-Cylinder Monitor

The geometry-dependent higher order contributions may be eliminated by clever design [1]. One such example is shown in Fig. 14. The charge induced on each detector half is again found by integrating the surface charge density:

$$Q_i = \frac{\lambda}{2}[L \pm \frac{r_0}{2\pi}\sin\phi_0\tan\theta] \tag{17}$$

where λ is the linear charge density, L is the total length of the detector, and ϕ_0 is the angular position of the charge relative to x=0. The angle θ denotes the angle of the cut measured from the vertical. The sensitivity of the split cylinder monitor is again determined by first evaluating the induced voltage. For long bunches, for which the signal is coupled out using a coaxial line, the capacitance C_e of the detector is $C_e=C/2$ where $C=L/Z_0c$ and Z_0 is the impedance of the coaxial line. With $i_w=\lambda c$ and since $\Delta x=r_0\cos\varphi_0$, the detected voltage is

$$V = \frac{2}{C_e}(Q_l - Q_r) = \frac{Z_0\tan\theta}{2\pi L}(-i_w)\Delta x \tag{18}$$

and the sensitivity is given by

$$S = \frac{Z_0 \tan\theta}{2\pi L} \tag{19}$$

The capacitive split cylinder is a linear detector; there are no geometry-dependent higher order contributions to the position sensitivity. The sensitivity is maximum for a cut angle of $\theta=\pi/4$.

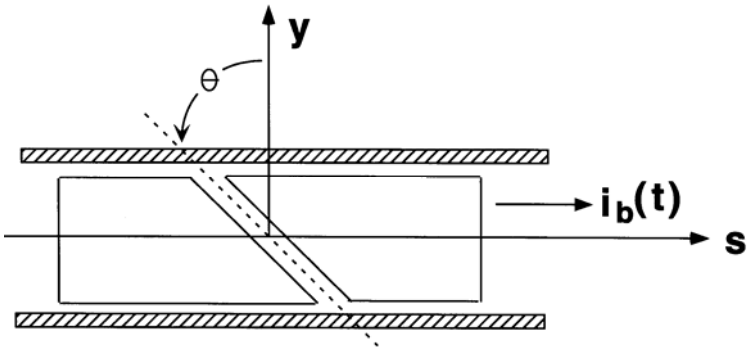

Fig. 14 Sketch of a split-cylinder capacitive monitor.

4.2.3 Button Monitors

Buttons are used frequently in sychrotron light sources and are usually terminated into a characteristic impedance consisting of a coaxial cable with an impedance of 50 Ω. A photograph of a button electrode for use between the undulators of the SASE FEL in the TESLA test facility is shown in Fig. 15 (from which it is clear from where buttons derive their name). A cross-sectional view of the BPM assembly used in the DORIS synchrotron light facility at DESY is shown in Fig. 16, which consists of 4 button electrodes. The design, which is similar to that used in the B-factories at SLAC and KEK, reflects geometrical constraints imposed by the vacuum chamber geometry (ease of vacuum chamber design). The nonlinear response for off-axis beams is often corrected for in software using simulations of the detector response.

Fig. 15 Button electrode from the Tesla Test Facility at DESY (courtesy D. Noelle and M. Wendt, 2003).

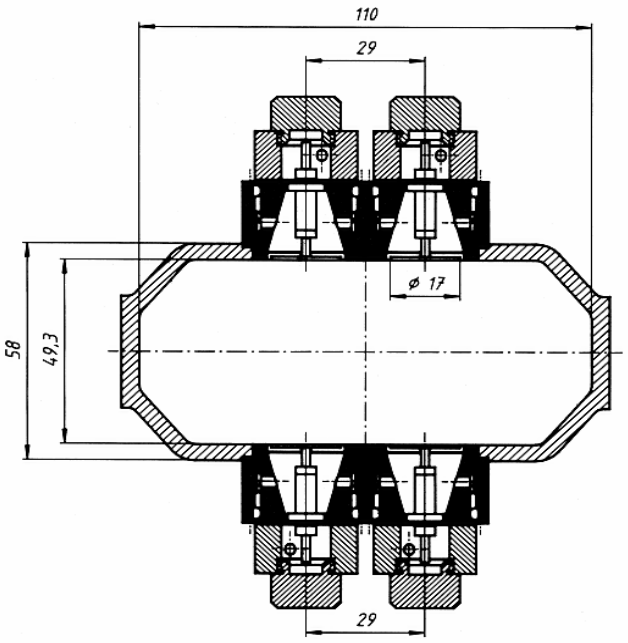

Fig. 16 Sketch of the BPM assembly from the DORIS synchrotron light facility at DESY (courtesy O. Kaul, 2003).

4.3 Beam Position – Stripline / Transmission Detectors

Transmission line detectors, often referred to by nature of their geometry as stripline detectors or in the literature occasionally as "wall-gap" monitors, are commonly used in both linear accelerators and storage rings. Two types of transmission line detectors are shown in Fig. 17. The darkened surfaces flush with the beam pipe represent the electrodes. The design concept relies on the coaxial structure of the beam pipe in which the electrode acts like the inner conductor of a coaxial line while the shield resembles the grounded outer conductor. The impedance of the coaxial line so formed[3] is Z_0. In Fig 17a, for example, the electrode is shorted to ground on the downstream end. Physically, the electrode may be welded to the vacuum chamber. The impedances (which are located physically outside of the vacuum chamber) denoted by R_L and R_R represent the output impedance of the detector. In Fig. 17b the electrode is appears to be suspended. In practice the electrodes are supported using nonconducting "stand-offs" or ceramics). A picture of a stripline BPM viewed from on-end is shown in Fig. 18.

In the following we calculate the sensitivity of the transmission line detector. The general case shown in Fig. 17b is analyzed followed by consideration of limiting cases. To determine the voltage generated at each resistor (R_L or R_R) the propagation of the beam-induced voltage along the electrode must be considered. We recall the following properties for the propagation of a signal through a characteristic impedance Z_0 terminated in a resistor R as sketched in Fig. 19. The reflection coefficient ρ is:

[3] This impedance is not to be confused with the impedance of output coupling, which may also consist of a coaxial cable, the impedance of which will be designated here by R.

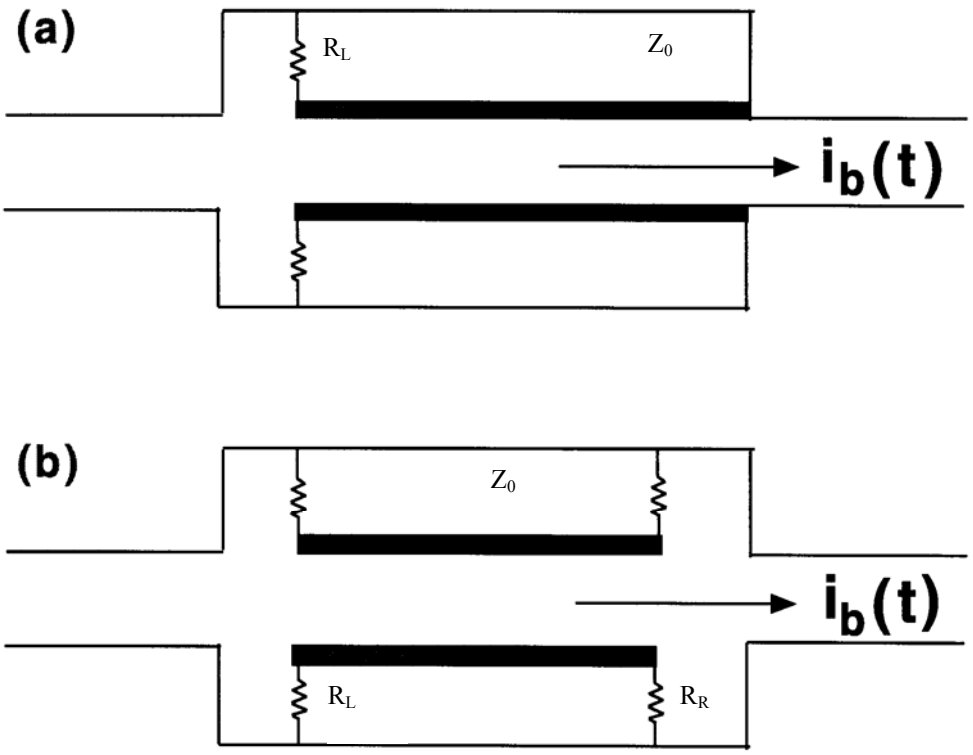

Fig. 17 Transmission line detector terminated on the right hand side to ground (a) and terminated into a matched impedance (b).

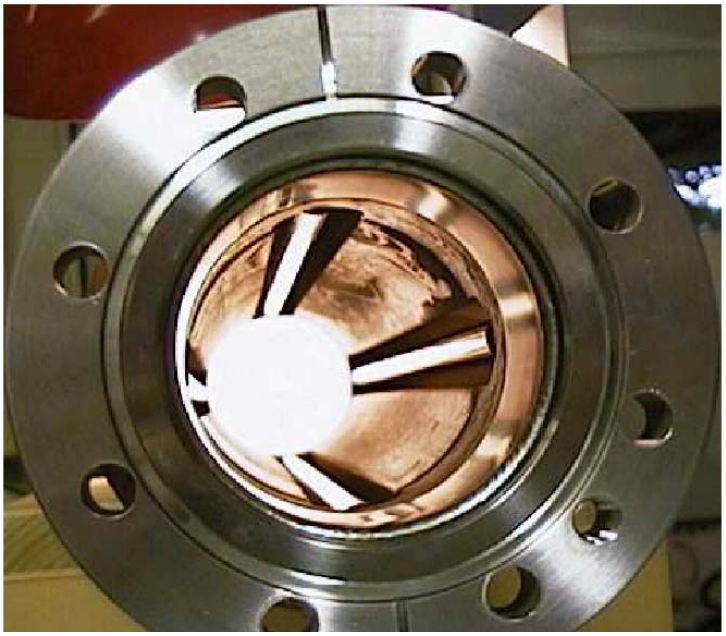

Fig. 18 Photograph of a stripline BPM from the HERA accelerator at DESY (courtesy M. Wendt, 2004).

$$\rho = \text{reflection coefficient} = \frac{R-Z_0}{R+Z_0} = \begin{cases} 0 & \text{if } R=Z_0 \\ -1 & \text{if } R=0 \\ >0 & \text{if } R>Z_0 \\ <0 & \text{if } R<Z_0 \end{cases} \tag{20}$$

while the transmission coefficient Γ is given by $\Gamma=\text{sqrt}(1-\rho^2)$.

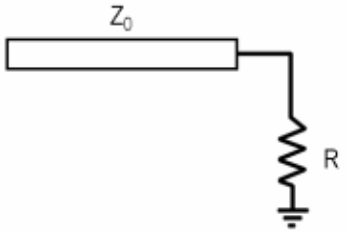

Fig. 19 Conceptual sketch of a coaxial line of impedance Z_0 terminated into an impedance R.

The equivalent circuit diagram for the terminated transmission line detector [16] is shown in Fig. 20. The voltage appearing across the resistors is evaluated by analyzing the current flow due to each gap. The problem will be simplified by assuming that the velocity of the wall current is equal to the velocity of the beam, which is approximately true in the absence of dielectrics and/or magnetic materials for relativistic beams. The time required for the beam to traverse the monitor is denoted by Δt (=L/c with L the electrode length and c the speed of light), which, in this approximation, is equal to the time required for the induced pulse to traverse the electrode. The notation used will be of the form $V_{RL,gL}$ which represents the voltage in R_L due to the signal generated at the left gap g_L. We assume that the beam travels from left to right as shown in Fig. 17.

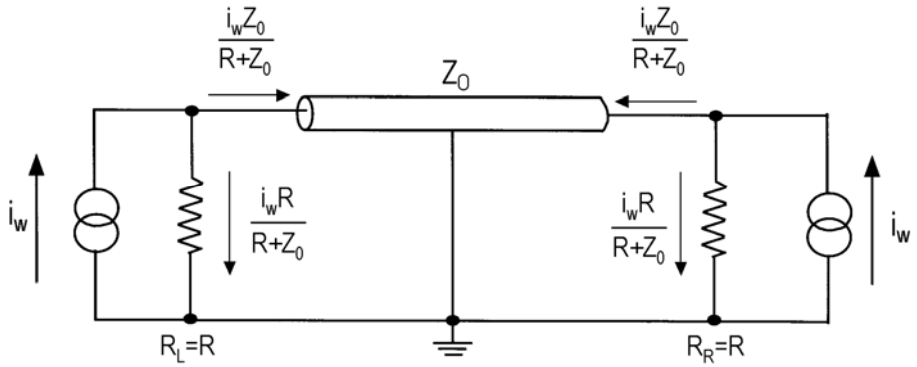

Fig. 20 Equivalent circuit for a transmission line detector.

The voltage appearing across R_L has two contributions arising from the contributions from each of the two gaps. The voltage generated by the first gap is

$$V_{R_L,g_L} = i_w\left[1+\left(\frac{R_R-Z_0}{R_R+Z_0}\right)e^{-2j\omega\Delta t}\right]\frac{R_L Z_0}{R_L+Z_0} \tag{21}$$

Where the first term is generated by the initial passage of the beam across the gap and the second term is the contribution from the first gap after the wave has propagated to the second gap and has been reflected back to the first gap (hence the factor of two for the total delay of 2Δt). In Eq. (21) we have for simplicity dropped the terms which are of higher order in the reflection coefficients (with time delays of 4,6,8,… times Δt) representing multiple reflections at the terminating impedances. The voltage appearing across R_L has also contributions arising from signals generated by the second gap:

$$V_{R_L,g_R} = -i_w e^{-j\omega\Delta t}\Big[1-(\frac{R_L-Z_0}{R_L+Z_0})e^{-j\omega\Delta t}\Big]\frac{R_L Z_0}{R_L+Z_0} \tag{22}$$

Here, the factor to the left of the square brackets (with time delay Δt) represents the current induced by the beam after having traversed the electrode. The remaining factor represents the transmission coefficient of the signal generated at the first gap (also with delay Δt). The total voltage appearing across R_L is $V_{RL}= V_{RL,gL} + V_{RL,gR}$.

Using the same logic as above, the voltage across R_R has two contributions. The voltage generated at the first gap is

$$V_{R_R,g_L} = i_w e^{-j\omega\Delta t}\Big[1-(\frac{R_R-Z_0}{R_R+Z_0})\Big]\frac{R_R Z_0}{R_R+Z_0} \tag{23}$$

where the first factor reflects the delay of the signal in reaching the gap and the second factor represents the transmission coefficient of the signal induced there. The voltage generated at the second gap is

$$V_{R_R,g_R} = -i_w e^{-j\omega\Delta t}\Big[1+(\frac{R_L-Z_0}{R_L+Z_0})e^{-2j\omega\Delta t}\Big]\frac{R_R Z_0}{R_R+Z_0} \tag{24}$$

where the first factor represents the delay of the beam, the first term in brackets gives the signal generated, and the second term in brackets corresponds to this signal after having been reflected back and forth from R_L. The total voltage appearing across R_R is $V_{RR}= V_{RR,gL} + V_{RR,gR}$.

We consider now special cases (with Δt=L/c):

(a) transmission line shorted to ground ($R_L=Z_0=R$, $R_R=0$) as in Fig. 17a

$$\begin{aligned} V_{R_L} &= \frac{i_w}{2}(1-e^{\frac{-2j\omega L}{c}})R \\ V_{R_R} &= 0 \end{aligned} \tag{25}$$

(b) transmission line terminated in a matched line ($R_L=R_R=Z_L$) as in Fig. 17b

$$\begin{aligned} V_{R_L} &= \frac{i_w}{2}(1-e^{\frac{-2j\omega L}{c}})Z_L \\ V_{R_R} &= 0 \end{aligned} \tag{26}$$

(c) transmission line with $R_L=R_R\neq Z_L$. In this case, the solutions for the voltages are the same as in (b) to second order in the reflection coefficient

Of the above cases, the transmission line shorted to ground is perhaps easiest to fabricate (the welds ensure better collinearity of the electrodes to the beam) and is most common. The transmission line terminated in a matched impedance, however, conveys directional information. In the example above, with the beam traveling from from gap 1 to gap 2, the right going wave from gap 1 cancels the left going wave from gap 2 at R_2. Likewise, for a beam traveling from gap 2 to gap 1 a voltage is detected at R_2 and not at R_1. Such a design was used at CERN in the SPS, which featured counter-rotating beams sharing a common vacuum chamber [1].

The sensitivity of the transmission line detector (single electrode) is given by

$$|S| = |\frac{V}{i_w}| = R|\sin^2\omega\Delta t| \tag{27}$$

As depicted in Fig. 21 for the case of an electrode of length L=10 cm. The signal peaks at an amplitude given by R at

$$\omega\Delta t = \frac{2\pi L}{\lambda} = \frac{\pi}{2} \tag{28}$$

that is, for an electrode length of λ/4 (which shows why such detectors are often referred to as "quarter-wave" detectors). The spacing between zeros is $\omega\Delta t=n\pi$ with integer n. We remark, that as before, the high frequency response in particular may be limited by the bandwidth of the signal processing electronics or, in this case, by the shunt capacitance of the resistors. Furthermore, in practice, bandpass filters are often added to reduce the power into the signal processors.

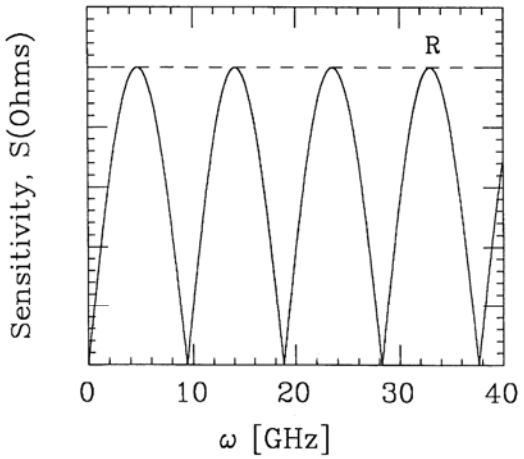

Fig. 21 Sensitivity of a quarter-wave transmission line detector with an electrode length of *l*=10 cm.

A photograph of a stripline monitor used at the LEUTL facility at Argonne is shown in Fig. 22. This shorted, S-band (2856 MHz), quarter-wave, four-plate detector was specially designed to enhance port isolation (using a short Tantalum ribbon to connect the stripline to the Molybdenum feedthrough connector) and to reduce reflections [17]. The electrode length is 28 mm (the electrical length used in circuit models, based on the measured response, was ~7% longer than the theoretical quarter-wavelength) and Z_0=50 Ω.

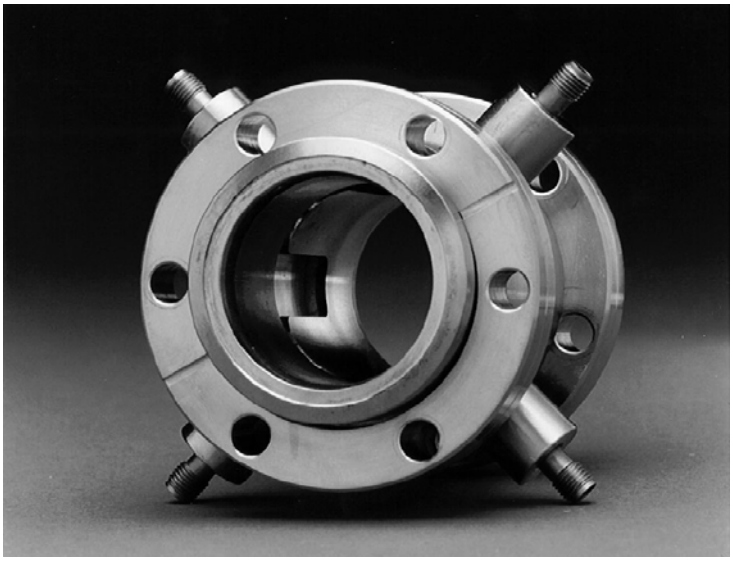

Fig. 22 Photograph of the shorted S-band quarter-wave four-plate stripline BPM used at in the SASE FEL facility LEUTL at Argonne (courtesy R. Lill, 2003).

4.4 Beam Position - Cavity BPMs [18]

Recently, resonant cavities have been developed for sub-micron measurements of the beam position in linear accelerators (as resonant devices, cavity BPMs are not suited for storage rings since signal amplitudes would be excessive). The growing interest in cavity BPMs is partially due to the proliferation of applications in microwave, as opposed to tranmission wave, technologies in industry. Pioneering experiments using 3 C-band "RF BPMS" placed sequentially, performed at the final focus test beam facility at Stanford, demonstrated a position resolution of 25 nm (at 1 nC bunch charge) [19,20], which exceeds substantially the sensitivity obtainable with the monitors described in the previous sections (comparison with the example of split-plate capacitive monitor terminated into 50 Ω, the cavity BPM offers a factor of 10^3 improved resolution).

The principle of the cavity BPM is excitation of discrete modes, which depend on the cavity geometry, the bunch charge q, the beam position δx, and the spectrum of the beam, which in turn depends on the bunch length, the bunch shape, and the spacing between bunches. A sketch of the measured electric fields generated in a simple pill-box type cavity is shown in Fig. 23 (left), from Ref. [18,21]. Shown are the fundamental mode (TM010 of amplitude A_{010} at frequency f_{010}), which is to be suppressed[4] by the processing electronics, and the dipole mode (TM110 of amplitude A_{110} at frequency f_{110}), e.g. position times charge, which is excited by an off-axis beam. Assuming perfect detector symmetry, the amplitude of the dipole mode is proportional to the beam offset. Representative signal amplitudes are shown in Fig. 23 (right). The signal is detected, in this example, using two antennas per plane of interest.

As before, the BPM sum and difference signals are used to determine the beam intensity and position. Assuming perfect detector symmetry, the BPM sum signal, with two antennas, is

$$V_1 + V_2 = 2 \times A_{010} \tag{29}$$

[4] see also Shintake, "common-mode-free BMPS" [22]

$$= 0 \times A_{110}$$

while the difference signal gives

$$V_1 - V_2 = 0 \times A_{010} \qquad (30)$$
$$= 2 \times A_{110}$$

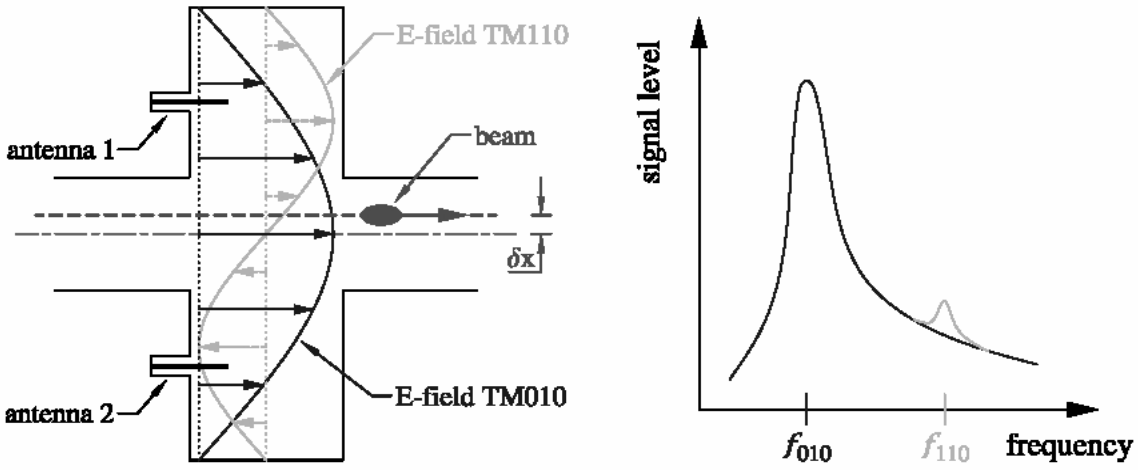

Fig. 23 Idealized sketch of excited fields in a cavity BPM due to an off-axis beam (left) and the corresponding frequency response (right) in a pill-box cavity BPM (from Ref. [18,20]).

Depending on the quality factor Q of the cavity, the detected signal may also contain information about (that is, be diluted by) the bunch structure (for cavities with high Q the signal decays slowly with decay time $\tau=2Q/\omega$); the cavity BPM is therefore best suited for widely separated bunches. On the other hand, the inherent symmetry of cavity BPMs offers better accuracy of absolute position (i.e. as compared to stripline monitors, geometrical defects during manufacture are less likely due to the improved mechanical rigidity) and so is the preferred choice of the SASE FEL of the LCLS facility to be built at Stanford [23], which is based on normal conducting cavities (with closely spaced, non-distinguishable bunches). For the European XFEL under consideration at DESY, which uses superconducting cavities for acceleration of the beam (thus allowing well separated bunches) so-called reentrant cavity BPMs (see next section) offering good sensitivity are being considered and have the advantage of resolving the position of every bunch.

Evaluation of the expected detector sensitivity is based, in the simplified case of the pill-box cavity, on solving Maxwell's equations for a cylindrical waveguide with perpendicular plates on the two ends [18]. In the following, we cite the results of Ref. [18,21]. Then issues of practical interest, based on the experiences at the Final Focus Test Facility at SLAC and the Tesla Test Facility at DESY, will be discussed. For the cylindrically symmetric pill-box BPM terminated into 50 Ω, the detected voltage V_{110}^{out} is related to the induced voltage V_{110}^{in} (both of mode 110 at frequency f_{110}) by [18]

$$V_{110}^{out}(\delta x) = V_{110}^{in}(\delta x)\left(\frac{R}{Q}\right)^{-\frac{1}{2}}\sqrt{\frac{50\Omega}{Q_L}}\sqrt{\frac{1-Q_L}{Q_0}} \qquad (31)$$

where δx is the transverse (in this case horizontal) position displacement, $(R/Q)_{110}$ is a geometrical factor depending on the impedance R and quality factor of mode 110, and Q_L is the

loaded quality factor related to the unloaded quality factor Q_0 by $Q_L = Q_0/(1+\beta)$, where β is the coupling coefficient for the 110 mode. With q the bunch charge, *l* the length of the cavity, r the cavity radius, the induce voltage is given by [21]

$$V_{110}^{in} \approx \delta x \cdot q \frac{l T_{tr}^{\ 2}}{r^3} \cdot 0.2474 \tag{32}$$

in units of Vm/pC. The transit time factor T_{tr} is given by

$$T_{tr} = \frac{\sin \eta}{\eta} \quad \text{with} \quad \eta = \frac{\pi l}{\lambda_{mn0}} \tag{33}$$

where λ_{mn0} is the wavelength of the mode of interest (in this case λ_{110}). For the cavity BPM tested at the TESLA Test Facility, shown in Fig. 24), with r=115.2 mm, L=52 mm, the position resolution is V_{110}^{out}~115 mV/mm at 1 nC.

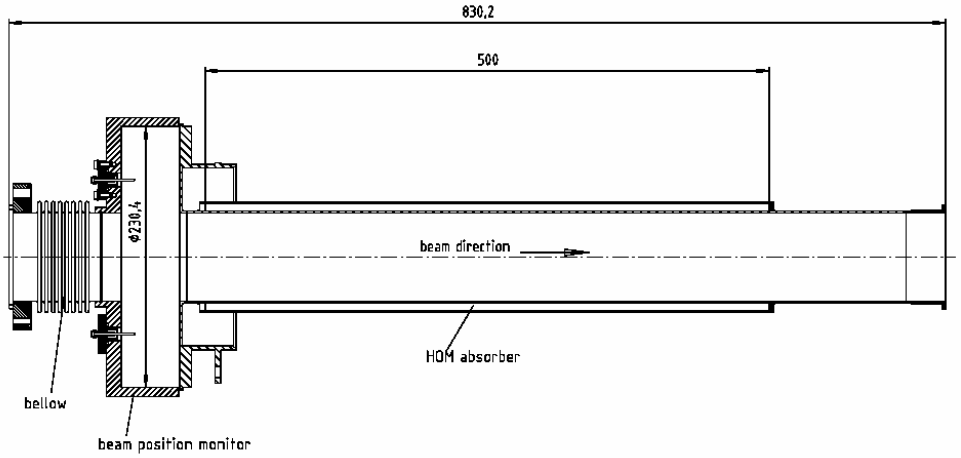

Fig. 24 Schematic of the "cold" cavity BPM (installed inside superconducting modules) tested at the TESLA test facility (from Ref. [21]).

In practice, small asymmetries in the antennas (or the wire loop pickups) arising for example from welding errors or improper alignment, becomes problematic. Tolerances on the asymmetry need to be quantified. The result is a distortion of the field lines which results in a slightly modified frequency f_{110} for the horizontal and vertical planes; i.e. the dipole mode signal appears to split into two peaks as detected in a single plane which makes signal interpretation difficult. A schematic of the serial cavity BPM assembly used in the above-mentioned pioneering experiment at the Final Focus Test Beam facility is shown in Fig. 25 [19,20]. Of particular note is the termination of the pick-up electrodes. To avoid electrode misalignments, small holes were drilled with high precision allowing insertion of the electrode thus better securing the overall geometry.

The resolution of the cavity BPM in the FFTB [19,20] was determined using the latter 3 BPMs (the phase cavity was used for synchronization). As shown in Fig. 26, the (in this case) vertical offsets of the first and third cavity BPMs were recorded. Given the absence of optical elements in the experimental geometry, the vertical beam position at the second cavity was directly inferred, given the known spatial separation between BPMs, using a linear fit (Fig. 26, top). This fitted value was then compared to the measured position at the second cavity (Fig. 26, bottom). Plotting the fitted position as a function of measured position at the middle cavity should ideally result in

a straight line with a 45º slope crossing through zero. The scatter of the resulting data points projected along this 45º axis gives a distribution with an rms value equal related to the BPM resolution as shown (corrected by a geometrical factor). With 1 nC bunch charge, these C-band cavity "RF BPMs" yielded a position resolution of a mere 25 nm. Perhaps of significance is the evidenced non-zero crossing of the fitted line which suggests a relative alignment error or electrical asymmetry.

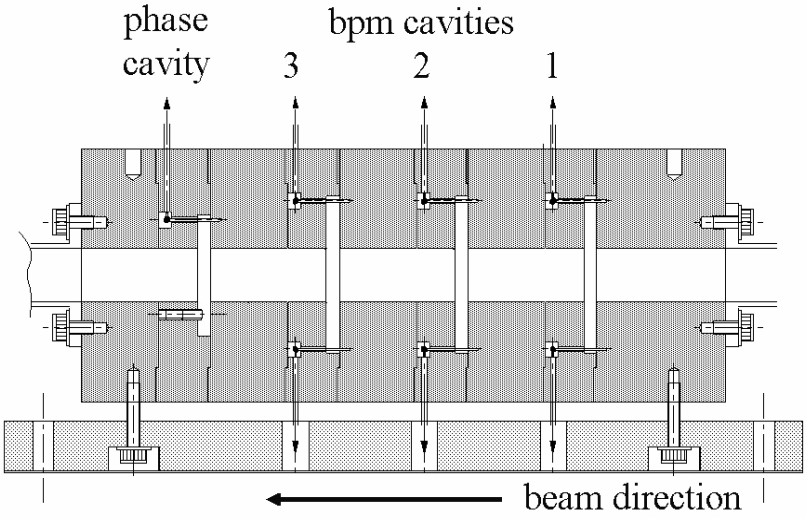

Fig. 25 Mechanical drawing of the triplet RF-BPM set (refered in this text as cavity BPMs) from the Final Focus Test Beam Facility (courtesy T. Shintake, 2003).

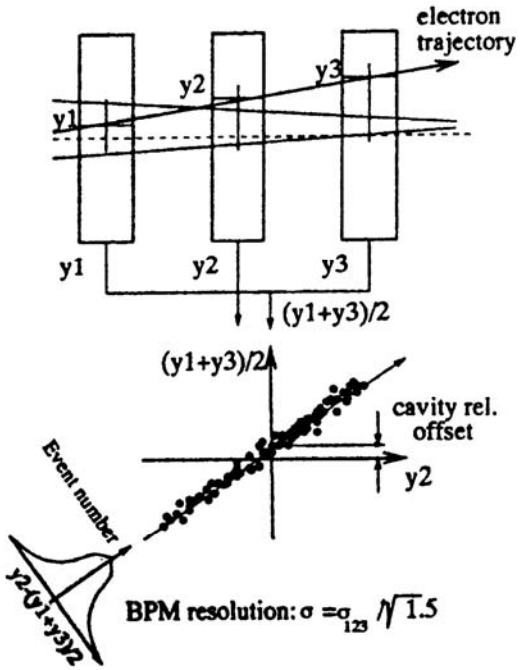

Fig. 26 Illustration of the C-band cavity BPM geometry used in the FFTB experiment at SLAC (top) and the method used to infer the resolution of the cavity BPM (bottom).

4.5 Beam Position – "Reentrant Cavity" BPMs [24]

The principle of so-called reentrant cavity BPMs is detection of an evanescent mode (TE011) of the cavity excited by a bunch with transverse displacement. In this case the cavity is excited at a frequency f_0 considerably below the resonant frequency of the cavity at frequency f_r. Even though the quality factor of the cavity decreases by sqrt(f_0/f_r), the attenuation constant for the evanescent fields below ~1/2 the cut-off frequency are practically constant allowing for reasonably high signal amplitude.

Shown in Fig. 27 is the cross-sectional view of the reentrant cavity BPM from Ref. [24]. The geometry is remarkably similar to that of the shorted transmission line. The equivalent circuit for the impedance model of this BPM was developed using URMEL [24]. Shown in Fig. 28 is the schematic for the reentrant cavity BPM used successfully at TTF-1 and planned for use at TTF-2 at the SASE-FEL facility at DESY [25].

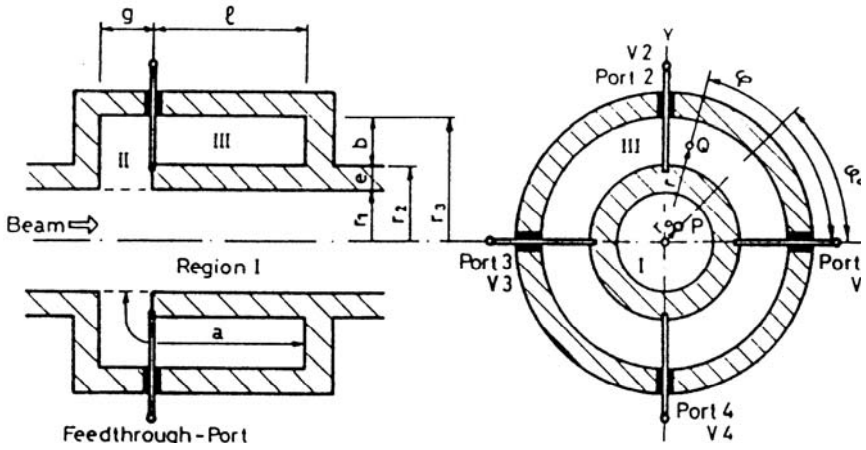

Fig. 27 Side view (left) and cross sectional view (right) of a reentrant cavity BPM developed at CERN [24].

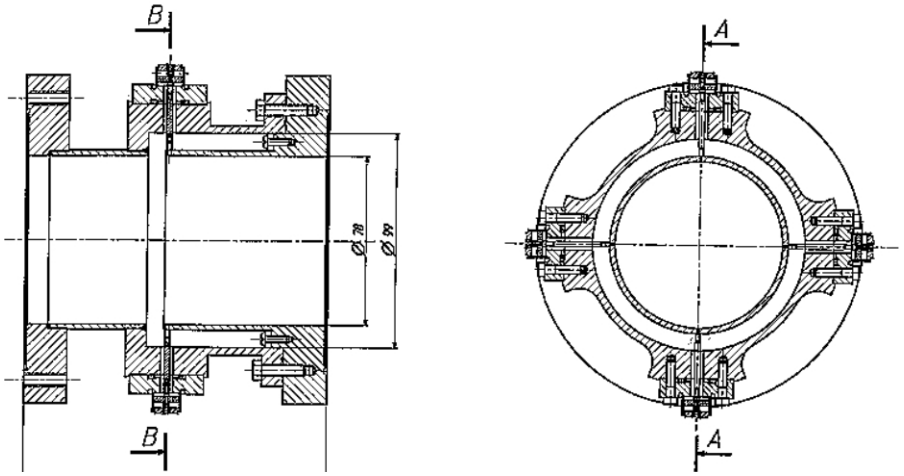

Fig. 28 Side view (left) and cross sectional view (right) of the reentrant cavity BPM used at the TESLA Test Facility (TTF-1) and planned for use at TTF-2 (courtesy C. Magne, 2003).

5. TRANSVERSE BEAM EMITTANCE

In this section we describe techniques for measuring the transverse emittances of the particle beam. We begin with a review of three equivalent and complementary methods for characterizing the second moments of the beam distribution and will refer to these later in the context of each application. The principles for measurement of the transverse beam emittance will be described for the (invasive) single quadrupole scan and for the (nominally noninvasive) method utilizing a minimum of 3 beam size measurements with illustrative examples from the SLC[5]. These methods rely on accurate beam size measurements. Measurement techniques for determining the beam size will be reviewed next with numerous examples from the Accelerator Test Facility (ATF) at KEK and the SLC.

5.1 Introduction

The determination of the transverse beam emittances may be characterized using at least 3 different equivalent formalisms: using the single-particle point-to-point transfer matrices, the transport of the Twiss parameters, or the transport of the so-called "beam matrix". In all cases we consider the ideal case of uncoupled motion (the horizontal and vertical degrees of freedom are independent of one another and of motion in the longitudinal plane).

(i) The transformation of the phase space coordinates (x, x') of a single particle from an initial to a final location (denoted by subscripts i and f, respectively) separated by some distance may be represented by a transport matrix, R as $X_f=RX_i$:

$$\begin{pmatrix} x \\ x' \end{pmatrix}_f = \begin{pmatrix} R_{11} & R_{12} \\ R_{21} & R_{22} \end{pmatrix}_{fi} \begin{pmatrix} x \\ x' \end{pmatrix}_i \tag{34}$$

where R is the point-to-point transfer matrix (obtained by multiplying the matrix representations of all elements between the initial and final observation points) and x is taken here to represent motion in either the horizontal or vertical plane. Averaging over all particles within the bunch, assuming that all the particles in the bunch move independently of one another, the first moment of the distribution $\langle x \rangle$ gives the mean position while the second moment of the distribution $\langle x^2 \rangle$ gives the transverse beam size since $\sigma_x=\langle x^2 \rangle^{1/2}$.

The first two moments of the distribution are given by:

$$\langle x \rangle = \frac{\int_0^\infty x f(x)\,\mathrm{d}x}{\int_0^\infty f(x)\,\mathrm{d}x} \qquad \text{and} \qquad \langle x^2 \rangle = \frac{\int_0^\infty x^2 f(x)\,\mathrm{d}x}{\int_0^\infty f(x)\,\mathrm{d}x} \tag{35}$$

where f(x) is the intensity distribution of the beam (which for lepton beams is usually taken to be Gaussian).

[5] The examples presented could be particularly useful for those involved in programming code as a performance check.

(ii) Equivalently, the Twiss parameters (α,β, and γ), which define the beam ellipse, obey

$$\begin{pmatrix}\beta\\ \alpha\\ \gamma\end{pmatrix}_f = \begin{pmatrix} R_{11}^2 & -2R_{11}R_{12} & R_{12}^2 \\ -R_{11}R_{21} & 1+2R_{12}R_{21} & -R_{12}R_{22} \\ R_{21}^2 & -2R_{21}R_{22} & R_{22}^2 \end{pmatrix}_{fi} \begin{pmatrix}\beta\\ \alpha\\ \gamma\end{pmatrix}_i \tag{36}$$

where in both cases above, the elements of the transfer matrix R are given generally by

$$\mathbf{R}_{fi} = \begin{pmatrix} \sqrt{\frac{\beta_f}{\beta_i}}(\cos\phi_{fi} + \alpha_i \sin\phi_{fi}) & \sqrt{\beta_f\beta_i}\,\sin\phi_{fi} \\ -\frac{1+\alpha_f\alpha_i}{\sqrt{\beta_f\beta_i}}\sin\phi_{fi} + \frac{\alpha_i-\alpha_f}{\sqrt{\beta_f\beta_i}}\cos\phi_{fi} & \sqrt{\frac{\beta_i}{\beta_f}}\,(\cos\phi_{fi} - \alpha_f \sin\phi_{fi}) \end{pmatrix} \tag{37}$$

If the initial (*i*) and final (*f*) observation points are the same, as for storage ring applications, then the matrix R is given by the one-turn-map R_{otm} as

$$\mathbf{R}_{\mathrm{otm}} = \begin{pmatrix} \cos\mu + \alpha\,\sin\mu & \beta\,\sin\mu \\ -\gamma\sin\mu & \cos\mu - \alpha\,\sin\mu \end{pmatrix} \tag{38}$$

where μ is the one-turn phase advance: μ =2πQ, where Q is the transverse betatron tune. Obtaining the beam size given the Twiss parameters will be shown after first introducing the beam matrix.

(iii) The beam matrix Σ_{beam} may be expressed either in terms of the Twiss parameters or in terms of the moments of the beam distribution as

$$\begin{aligned}\Sigma^x_{\mathrm{beam}} &= \epsilon_x \begin{pmatrix} \beta & -\alpha \\ -\alpha & \gamma \end{pmatrix} \\ &= \begin{pmatrix} \langle x^2\rangle - \langle x\rangle^2 & \langle xx'\rangle - \langle x\rangle\langle x'\rangle \\ \langle x'x\rangle - \langle x'\rangle\langle x\rangle & \langle x'^2\rangle - \langle x'\rangle^2 \end{pmatrix}\end{aligned} \tag{39}$$

The transformation of an initial beam matrix $\Sigma_{beam,0}$ to the desired observation point is

$$\Sigma_{\mathrm{beam}} = R\Sigma_{\mathrm{beam},0}R^t \tag{40}$$

where R is again the transfer matrix given in Eq. (34). Neglecting the mean of the distribution, that is, disregarding the static position offset of the core of the beam; i.e. <x>=0, then

$$\Sigma^x_{\mathrm{beam}} = \begin{pmatrix} \langle x^2\rangle & \langle xx'\rangle \\ \langle xx'\rangle & \langle x'^2\rangle \end{pmatrix} \tag{41}$$

and the beam size is given by the root-mean-square (rms) of the distribution: $\sigma_x=<x^2>^{1/2}$. The beam emittance ε is given from the determinant of the beam matrix:

$$\epsilon_x = \sqrt{\det\ \Sigma^x_{\text{beam}}} \tag{42}$$

with

$$\det\ \Sigma^x_{\text{beam}} = \Sigma_{11}\Sigma_{22} - {\Sigma_{12}}^2 \tag{43}$$

5.2 Determination of the transverse beam emittance

In transport lines and linear accelerators the beam emittances are often measured using one of two favored techniques: the quadrupole scan or the multi-wire/multi-screen method. The latter may often be executed in a parasitic way since the magnetic optics are not changed (however, at the expense of the additional hardware requirements), while the quadrupole scan perturbs the beam (and could result in beam loss in downstream systems).

5.2.1 The quadrupole scan [26]

The measurement setup depicted schematically together with the notation for the transfer matrix elements is shown in Fig. 29. Here Q represents the transfer matrix of the quadrupole, S the transfer matrix of the space between the quadrupole and the beam size detector (which consists of the matrix product of all the optical elements including drifts and quadrupoles, etc.), and R=SQ denotes the total transfer matrix. Optimally the setup of the experiment is such that S is given by a pure drift space so that the measurements are least susceptible to modeling errors in any additional optical components. The observable of interest is the beam size, which is to be measured as a function of the quadrupole field strength. We assume that the measurement is conducted with a well-centered beam (that is, as the current in the quadrupole is changed, the beam position remains constant – i.e. doesn't incur a dipole kick due to feeddown[6] in the quadrupole).

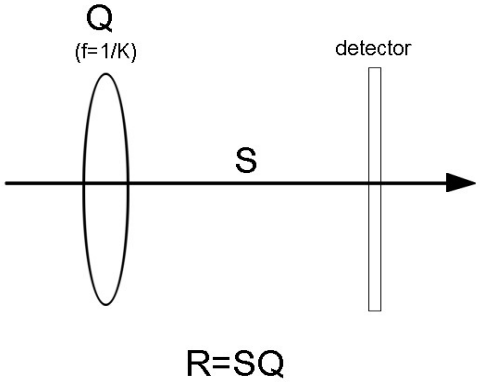

Fig. 29 Sketch of the layout of a quadrupole scan used in measurement of the transverse beam emittances.

[6] Here "feeddown" refers to the next lower-order field that a beam experiences by being off-axis in a multipole of order n; i.e. a quadrupole (and dipole) field if off-axis in a sextupole, or in this case, a dipole field if off-axis in a quadrupole.

Using a thin-lens approximation for the quadrupole with K=±1/f, where f is the focusing strength of the quadrupole (- for focusing and + for defocusing), then

$$Q = \begin{pmatrix} 1 & 0 \\ K & 1 \end{pmatrix} \quad \text{and} \quad R = \begin{pmatrix} S_{11} + KS_{12} & S_{12} \\ S_{21} + KS_{22} & S_{22} \end{pmatrix} \tag{44}$$

Expanding the position function from Eq. (34), the (11)-element of the beam transfer matrix, Eq. (41), after some algebra, is found to be quadratic in the field strength K:

$$\begin{aligned} \Sigma_{11}(=\langle x^2 \rangle) = &({S_{11}}^2 \Sigma_{11_0} + 2S_{11}S_{12}\Sigma_{12_0} + {S_{12}}^2 \Sigma_{22_0}) \\ &+ (2S_{11}S_{12}\Sigma_{11_0} + 2{S_{12}}^2 \Sigma_{12_0})K + {S_{12}}^2 \Sigma_{11} K^2 \end{aligned} \tag{45}$$

Measurements of the beam size versus quadrupole field strength from the SLC are shown in Fig. 30 taken from the transfer line between the electron damping ring and the main linac.

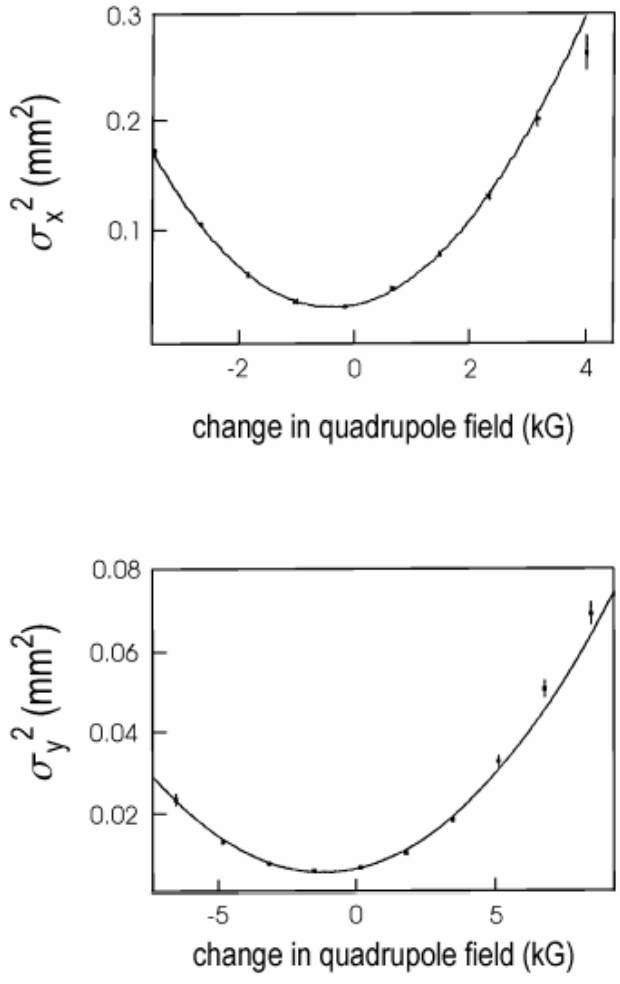

Fig. 30 Measurements of the transverse beam emittance at the SLC using the method of the quadrupole scan.

The parabolic fitting function in Fig. 30 is of the form

$$\begin{aligned}\Sigma_{11} &= A(K-B)^2 + C \\ &= AK^2 - 2ABK + (C + AB^2)\end{aligned} \tag{46}$$

Equating terms in Eqs. (45) and (46) and dropping the 'o' subscipts, we have

$$\begin{aligned}A &= S_{12}^2 \Sigma_{11}\,, \\ -2AB &= 2S_{11}S_{12}\Sigma_{11} + 2S_{12}^2\Sigma_{12}\,, \\ C + AB^2 &= {S_{11}}^2\Sigma_{11} + 2S_{11}S_{12}\Sigma_{12} + {S_{12}}^2\Sigma_{22}\end{aligned} \tag{47}$$

which represents 3 equations with 3 unknowns given by the fit parameters A, B, and C. Solving for the elements of the beam matrix,

$$\begin{aligned}\Sigma_{11} &= A/{S_{12}}^2\,, \\ \Sigma_{12} &= -\frac{A}{{S_{12}}^2}\left(B + \frac{S_{11}}{S_{12}}\right)\,, \\ \Sigma_{22} &= \frac{1}{{S_{12}}^2}\left[(AB^2 + C) + 2AB\left(\frac{S_{11}}{S_{12}}\right) + A\left(\frac{S_{11}}{S_{12}}\right)^2\right]\end{aligned} \tag{48}$$

The beam emittance, given by the determinant of the beam matrix, Eq. (42), is then obtained directly from the fit parameters:

$$\epsilon_x = \sqrt{AC}/S_{12}^2 \tag{49}$$

Likewise, using the definition of the Twiss parameters in terms of the beam matrix elements, Eq. (39), the 3 Twiss parameters, and hence the orientation of the beam in phase space, as shown in Fig. 31, are known. Namely,

$$\begin{aligned}\beta_x &= \frac{\Sigma_{11}}{\epsilon} = \sqrt{\frac{A}{C}}\,, \\ \alpha_x &= -\frac{\Sigma_{12}}{\epsilon} = \sqrt{\frac{A}{C}}\left(B + \frac{S_{11}}{S_{12}}\right)\,, \\ \gamma_x &= \frac{{S_{12}}^2}{\sqrt{AC}}\left[(AB^2 + C) + 2AB\left(\frac{S_{11}}{S_{12}}\right) + A\left(\frac{S_{11}}{S_{12}}\right)^2\right]\end{aligned} \tag{50}$$

As a useful check, the beam-ellipse parameters should satisfy the fundamental relationship for the Twiss parameters: $(\beta\gamma\text{-}1)=\alpha^2$. If this relationship does not hold given the Twiss parameters derived from the fit, then reasons must be investigated. A likely source for discrepancy (as

experienced in practice) is the error introduced by the thin-lens approximation for the quadrupole[7].

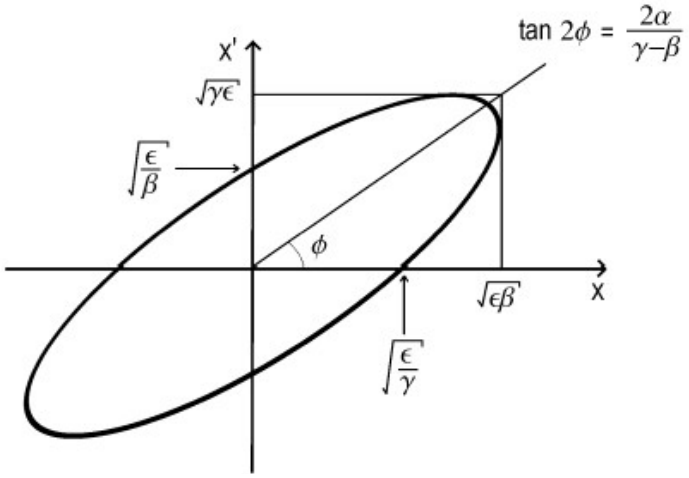

Fig. 31 Beam ellipse in transverse phase space in terms of the Twiss parameters.

5.2.2 Multiple wire (or screen) measurement of the beam emittance [27,28]

The measurement geometry for measuring the beam emittance using multiple measurements of the beam size is depicted in Fig. 32. The syntax used is: superscripts to denote the "measurement number", or location, and subscripts to designate the matrix elements for the transfer matrix of interest.

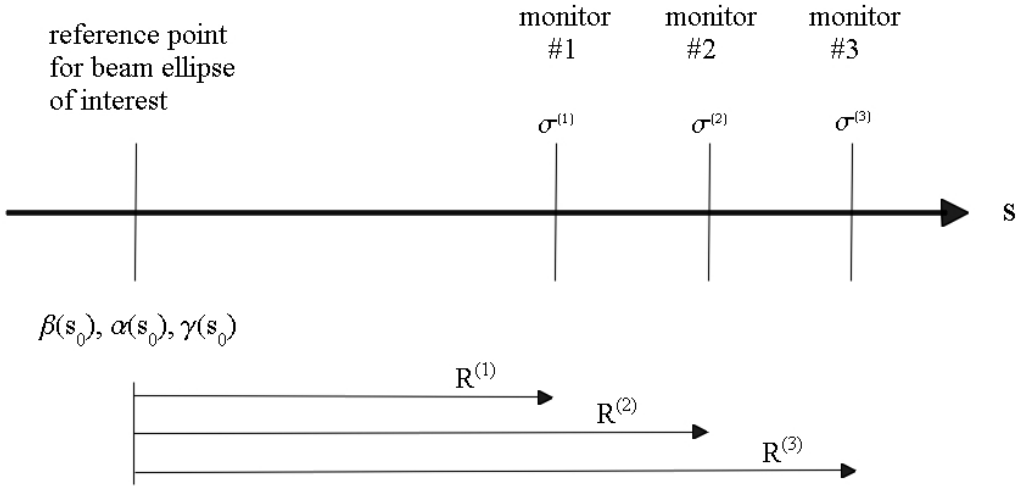

Fig. 32 Geometry of the multiple wire/screen method for measurement of the transverse beam emittances.

[7] The exact matrix representation for a quadrupole, obtained by solving Hill's equation, may be found in Ref. [28], for example.

Referring to Fig. 32, with fixed optics and multiple (total of n) measurements of the horizontal beam size σ_x at the different locations along the beamline, we may write:

$$\underbrace{\begin{pmatrix} (\sigma_x{}^{(1)})^2 \\ (\sigma_x{}^{(2)})^2 \\ (\sigma_x{}^{(3)})^2 \\ \cdots \\ (\sigma_x{}^{n})^2 \end{pmatrix}}_{\Xi_x} = \underbrace{\begin{pmatrix} (R_{11}{}^{(1)})^2 & 2R_{11}^{(1)}R_{12}^{(1)} & (R_{12}{}^{(1)})^2 \\ (R_{11}{}^{(2)})^2 & 2R_{11}^{(2)}R_{12}^{(2)} & (R_{12}{}^{(2)})^2 \\ (R_{11}{}^{(3)})^2 & 2R_{11}^{(3)}R_{12}^{(3)} & (R_{12}{}^{(3)})^2 \\ \cdots & & \\ (R_{11}{}^{(n)})^2 & R_{11}^{(n)}R_{12}^{(n)} & (R_{12}{}^{(n)})^2 \end{pmatrix}}_{\mathbf{B}} \underbrace{\begin{pmatrix} \beta(s_0)\epsilon \\ -\alpha(s_0)\epsilon \\ \gamma(s_0)\epsilon \end{pmatrix}}_{\mathbf{o}} \tag{51}$$

The optimum wire locations for maximum sensitivity are such that the separation between wires corresponds to a difference in betatron phase advance i(180º/(n+1)) where the number of measurement n must be at least 3 (to solve for the 3 unknowns) and i=0,1,…,n.

Using the symbol definitions shown in Eq. (51), the matrix equation to be solved is

$$\Xi_x = \mathbf{B} \cdot \mathbf{o} \tag{52}$$

The solution for the vector with the Twiss parameters is given by minimizing the sum (this is a least squares fit)

$$\chi^2 = \sum_{l=1}^{n} \frac{1}{\sigma^2_{\Xi_x^{(l)}}} \left(\Xi_x^{(l)} - \sum_{i=1}^{3} B_{li} o_i \right)^2 \tag{53}$$

Where $\sigma_{\Xi x^{(l)}}$ denotes the error of $\Xi_x{}^{(l)}=(\sigma_x{}^{(l)})^2$ (i.e. this is the error in the Gaussian fit for wire *l*). Forming a symmetric n x n covariance matrix

$$\mathbf{T} = (\hat{\mathbf{B}}^t \cdot \hat{\mathbf{B}})^{-1} \tag{54}$$

the least-squares solution to Eq. (54) is

$$\mathbf{o} = \mathbf{T} \cdot \hat{\mathbf{B}}^t \cdot \hat{\Xi}_x \tag{55}$$

with dimension of (3 by 1) independent of the number of measurements. Equation (55) yields the Twiss parameters of interest in terms of the measured beam sizes and the beam optics, which are assumed to be known. Here the 'hats' show the weighting used in the normalization so that the rms error is 1:

$$\hat{\Xi}_x^{(l)} = \frac{\Xi_x^{(l)}}{\sigma_{\Xi_x^{(l)}}} \qquad \text{and} \qquad \hat{B}_{li} = \frac{B_{li}}{\sigma_{\Xi_x^{(l)}}} \tag{56}$$

Once the components of the vector with the Twiss parameters is known, the emittance and Twiss parameters are given by

$$\begin{aligned} \epsilon &= \sqrt{o_1 o_3 - o_2^2} \\ \beta &= o_1/\epsilon \\ \alpha &= -o_2/\epsilon \end{aligned} \tag{57}$$

and $\gamma=(1+\alpha^2)/\beta$. Raw beam size data obtained using wire scanners in the injector linac of the SLC are shown in Fig. 33. We intentionally show this particularly poor set of data to illustrate the usefulness of a graphical summary (see below) of the measurement as shown in Fig. 34.

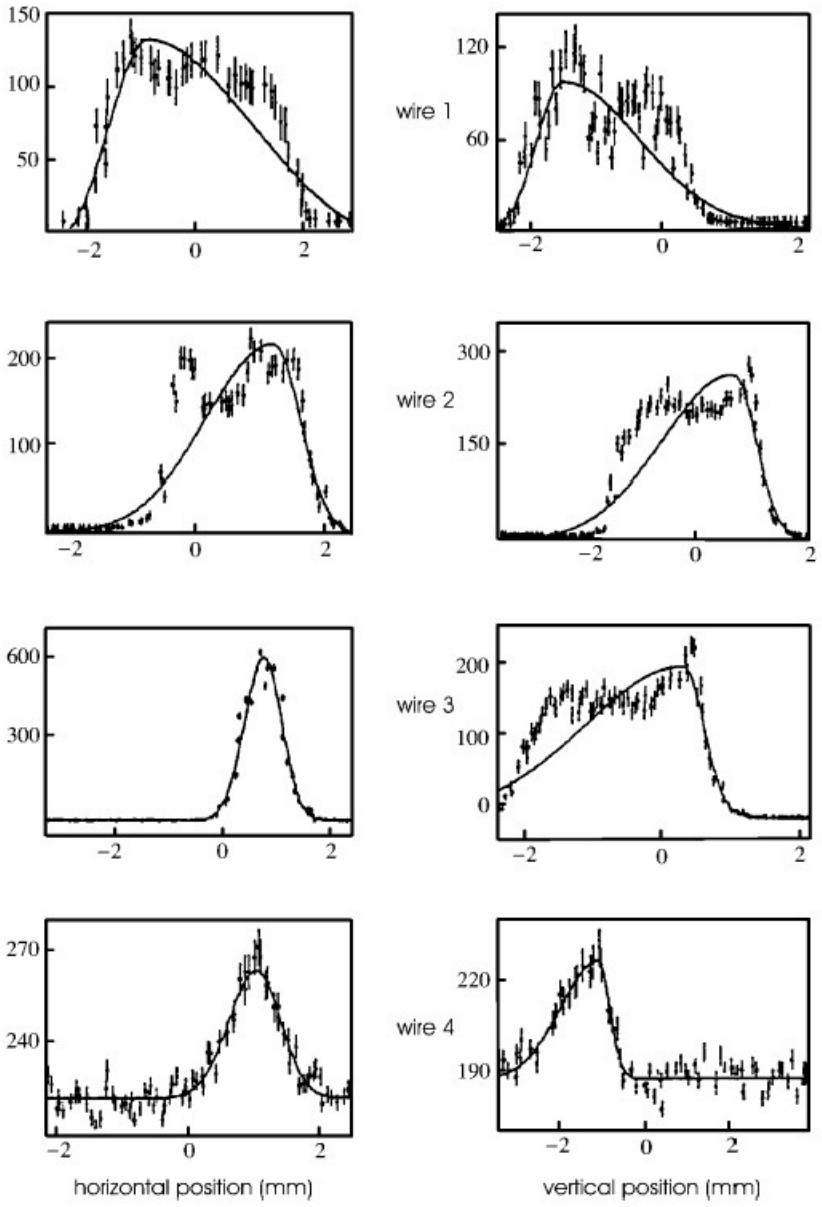

Fig. 33 Wire scanner data measured in 4 different locations in the injector linac at the SLC.

The beam size measurements in Fig. 33 are clearly non-Gaussian. This is usually not the case for measurements in a transport line (or linear accelerator) following a storage ring but is not unusual in low energy linear accelerators. The fits in the case shown are "bi-Gaussian"; that is, each side of the profile is fitted independently with a Gaussian (giving standard deviations σ_L on the left and σ_R on the right). For insertion into the Ξ-matrix above the mean, $\sigma=(\sigma_L+\sigma_R)/2$, is used. This fitted σ therefore, while 'representative' of the distribution, is not equivalent to the true rms of the distribution (which one would have with perfect Gaussian profiles). However, experience has shown that even an approximate way of characterizing the data is useful for either monitoring purposes or in efforts aimed towards improving the beam quality.

The data may be represented graphically in the following convenient way as shown in Fig. 34. Since the Twiss parameters at the point of interest are known, the ellipse in phase space (x, x') as in Fig. 31 may be reconstructed. Alternatively, the ellipse may be plotted in normalized phase space (x, $p_x=\alpha_x x+\beta_x x'$) where p_x is canonically conjugate to x. A further refinement is to normalize both coordinates to the square root of the beta function at the reference point for the beam ellipse of interest so that the design ellipse has unity radius in these coordinates. That is, for the graphical representation, plot the design ellipse and the measured ellipse as represented by

$$\left(\frac{x}{\sqrt{\beta_x}}, \frac{\alpha_x x+\beta_x x'}{\sqrt{\beta_x}}\right) \tag{58}$$

In addition, it is of interest to plot the wires mapped back to the observation point using

$$\begin{pmatrix} x \\ x' \end{pmatrix}_{\text{ref point}} = R^{-1}\begin{pmatrix} \sigma_{x,w} \\ x'_w \end{pmatrix} \tag{59}$$

For example, two measurements separated by 90º phase advance would be instantly visible as two lines intersecting also at a 90º angle.

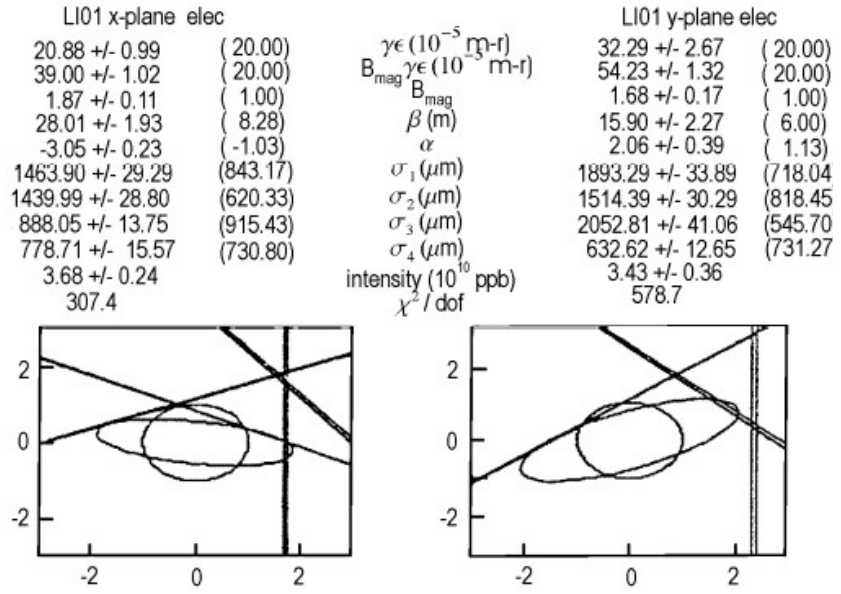

Fig. 34. Graphical representation of the emittance measurement.

The utility of the graphical representation is now clear: 1) The fact that the design ellipse (circle in this normalized phase space) and the measured ellipse are not both round indicates what is refered to as a "mismatch"[8] [29]; 2) At a glance, the phase space coverage of the beam size measurements is immediately clear: we observe, for the case of the horizontal plane shown on the left, phase advances of 0º, ~45º, ~67.5º , and ~(90+22.5º); 3) whereas only 3 measurements are required to determine the Twiss parameters, a fourth measurement has been included (in the case of the measurement of the horizontal emittance). However, we observe that 1 of the 4 wires does not touch the measured beam ellipse thus indicating an optical error (in this case the data from this wire is best omitted when determining the Twiss parameters, as was done for the vertical beam emittance measurement). In the text display of Fig. 31 is included also for convenience the design beam sizes and the design Twiss parameters at the point of interest as well as the beam intensity (in units of particles per bunch, ppb) and the goodness of fit indication, the χ^2.

Lastly we remark, that in the design of a multiple wire or screen emittance station, by clever choice of the optical parameters at the location of the measurements, even more information could be inferred from the graphical representation. For example, suppose that the design β-functions at two of the wires are equal and that the measured beam sizes are different. In the absence of an optical error, this could indicate a dispersive contribution to the beam size.

5.3 Measurements of the transverse beam size

The emittance measurements described in the preceding section rely on accurate measurements of the beam size. In this section we describe the hardware used for measuring the beam size including directly intercepting screens, transition radiation (favored conventionally in transport lines and linear accelerators), conventional wire scanners and laser wire scanners (applicable in linear lattices or circular accelerators). To complement the lectures presented by A. Hoffmann, various measurements based on measurements of the emitted synchrotron radiation in storage rings are described.

5.3.1 Measurement of the transverse beam size using screens

A schematic view of a vacuum chamber and hardware associated with beam size measurement utilizing a screen is shown [30] in Fig. 35. The intercepting screen (composed for example of Al_2O_3Cr possibly with a phosphorescent coating) is inserted, usually at a 45º angle (to simplify the vacuum chamber geometry) into the path of the beam. The image is then viewed by a camera allowing direct observation in the horizontal and vertical planes (x-y) in locations of zero dispersion ($\eta=0$) for which the beam position is independent of beam energy, or in the energy and vertical planes (δ-y) in regions of nonzero dispersion ($\eta \neq 0$). Orientation of the camera for head-on viewing of the screen is advisable in order to avoid corrections (path-length dependent aberrations in the camera lenses) as illustrated by the orientation of the view port in Fig. 35.

R. Jung et al, in Ref [31] have defined the following characteristics[9] of light emission from the screen: fluorescence – referring to light emitted on short time scales (t~10 ns) as the atoms in the screen excited by the beam decay back to their ground state, phosphorescence – light continues to be emitted (t~μs) after the exciting mechanism has ceased[10], and luminescence – a combination of both processes.

---

[8] The mismatch parameter denoted in the text of Fig. 34 by B_{mag} is unity for perfectly matched beams or >1 if mismatched. The physical interpretation is that the beam, if allowed to filament completely after propagating through identical lattice sections, would have an emittance then equal to $B_{mag}\varepsilon$, where ε denotes the emittance just measured.

[9] The definitions are useful given that the words fluorescence, phosphorescence, and luminescence seem to be used somewhat randomly in the literature.

[10] For example, "afterglow" in analogue oscilloscopes.

In the beam size measurement utilizing screens, the image is digitized, projected onto orthogonal axes, and fitted with a Gaussian function. A "background image" (obtained without beam) is subtracted from the data (here line-locking of the camera may be important). The calibration may be most easily obtained using as reference grid lines etched directly on the screen or from drilled calibration holes either of which has a known spacing.

Special concerns for beam size measurements utilizing screens include the special resolution (of typically 20-30 μm) given by the phosphor grain size and transparency, the temporal resolution given by the decay time, radiation hardness of the screen and camera, and the dynamic range (i.e. saturation of the screen at high beam currents).

At the SLC the beam sizes at the end of the 50 GeV lepton linac were routinely monitored using screens [32]. Rather than inserting a screen directly into the beam path, fast kicker magnets (2 per plane) were used to deflect the bunch of interest onto dedicated screens. An example of such measurements is shown in Fig. 36.

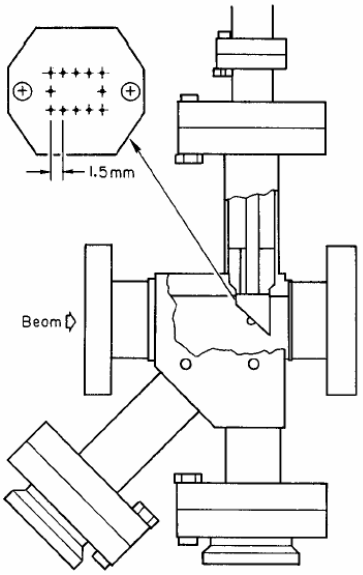

Fig. 35 Beam size measurement assembly utilizing a screen (courtesy P. Tenenbaum, 2003).

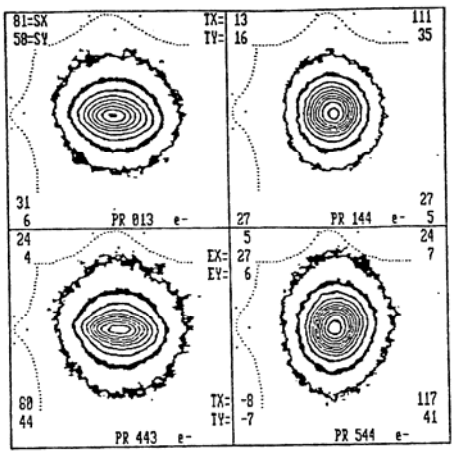

Fig. 36 Beam size monitoring using screens at the end of the SLC linac (courtesy F.J.-Decker, 2004).

5.3.2 Measurement of the transverse beam size using optical transition radiation (OTR)

When a charged particle crosses between two materials of different dielectric constant (for example, between vacuum and a conductor), transition radiation is generated. The time dependence of the photon emission is short (~1 ps) allowing for temporal resolution of closely spaced bunches. Beam profiling using OTR are reviewed, for example, in Refs. [33-35].

The radiation from the foil is emitted in both the forward and backward directions as shown [36] in Fig. 37 for the case of a foil oriented at 45º with respect to the incident beam. Represented schematically are lobes of peak intensity (strongest electric field of the emitted photon beam). These lobes are centered about the direction of the beam for the case of forward transition radiation and about an axis that obeys Snell's law (of equal angle of incidence and reflection) for the backward transition radiation. While the optimum viewing angle for minimum systematic distortion is such that the camera lenses are flush with the screen, the radiation emitted at a 90º angle with respect to the beam is often viewed since there the light intensity is highest. Aberrations in the camera lenses must in such a case be taken into account. In certain applications, the image plane of the camera is tilted to avoid such aberrations.

Typical compositions of the foil for OTR measurements are Al, Be, Si, or Si with an Al coating. Similarly to beam size measurements using screens, the images obtained are digitized and fitted using typically a Gaussian distribution and the calibration is often obtained using etched lines of known spacing.

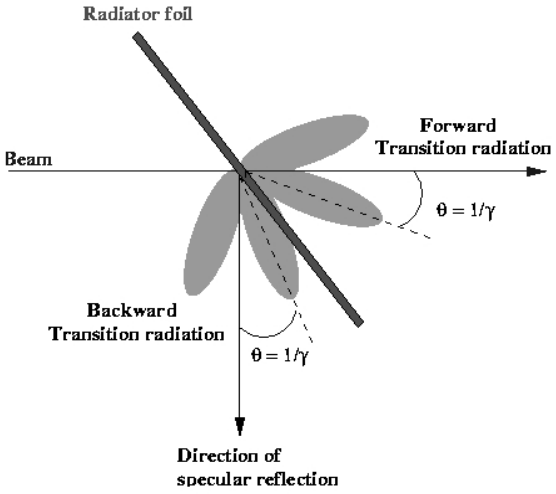

Fig. 37 Conceptual view of emitted optical transition radiation generated by a beam striking a thin foil (courtesy K. Honkavaara, 2003).

Issues related to beam size measurements using optical transition radiation include the special resolution (the upper limit of which was thought, based on literature, to be higher than that recently demonstrated, see below, but is widely considered to be ~5 μm), damage to the radiator, particularly in the case of small beam sizes, and as mentioned, geometrical depth-of-field effects resulting from the geometry associated with imaging the backward transition radiation. As in the case with normal screens, background subtraction is also of critical importance.

Recently, a resolution of 1 μm was demonstrated [37] in an OTR measurement at the accelerator test facility (ATF) at KEK. The vertical beam size of about 5 μm was measured at the exit of the low-emittance damping ring in the downstream transfer line. The measurement setup

is shown in Fig. 38 and includes a Cu target, a 1 mm exit window (with a surface flatness given by the pressure differential across the window of about λ/4), and an imaging system with a triggered CCD camera (with a pixel size of 10 μm). The geometry was optimized, within the mechanical constraints and at the expense of intensity, to try to achieve normal incidence of the camera on the target. To minimize the possible systematic error resulting from the change in focal depth with position on the target, rather than tilting the image plane of the camera, the field of view was made to be narrow. An example of the beam size measured using this SLAC-built OTR station at the ATF [37] is shown in Fig. 39.

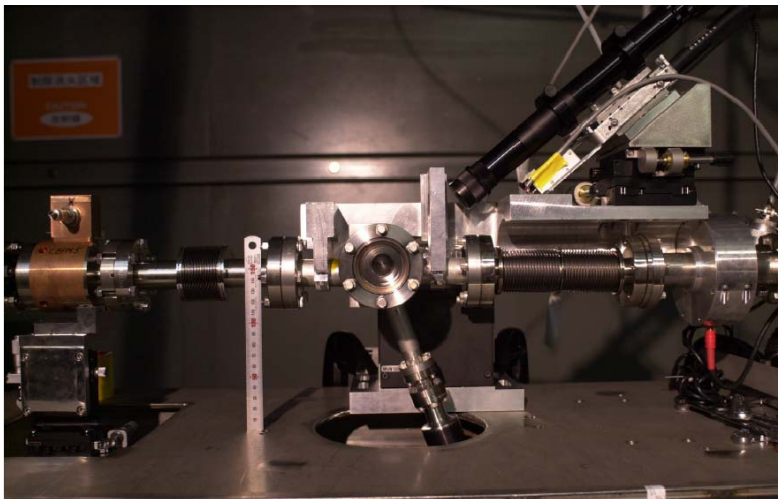

Fig. 38 Photograph of the optical transition radiation hardware for measurement of the beam size as mounted in the extraction line of the ATF damping ring (courtesy M. Ross, 2003).

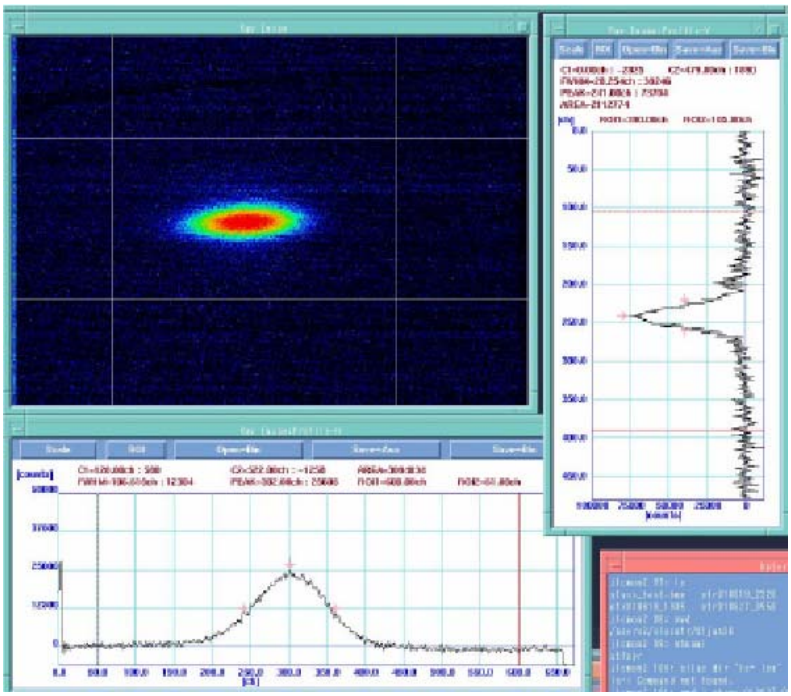

Fig. 39 Beam size measurement at the ATF using optical transition radiation (courtesy M. Ross, 2003).

5.3.3 Measurement of the transverse beam size using (conventional) wire scanners

Wire scanner measurements (see for example Refs. [38-39]) may be used usually noninvasively in both linear and circular lepton accelerators. The wire is mounted rigidly on a shaft which is moved using a precision stage with a precision encoder. Usually the wire (e.g. of material C, Be, or W) is moved across the beam. In certain cases, the beam is moved across the wire (which no longer constitutes a noninvasive measurement if the change in beam position is not compensated for downstream). A typical support structure for wires is shown in Fig. 40 for the scanner assembly in the extraction line of the accelerator test facility at KEK [40]. With the scanner mounted at 45º with respect to the beamline, the horizontal/vertical wire is used for measurements of the vertical/horizontal beam sizes respectively. The wire mounted at 45º is used to infer the coupling (with 45º optimal for the case of a round beam). The precision of the stepper-motor in this assembly was 0.5 μm. The optimum velocity of the wire passage through the beam depends on the desired interpoint spacing and on the bunch repetition frequency (as constrained possibly by beam-induced heating).

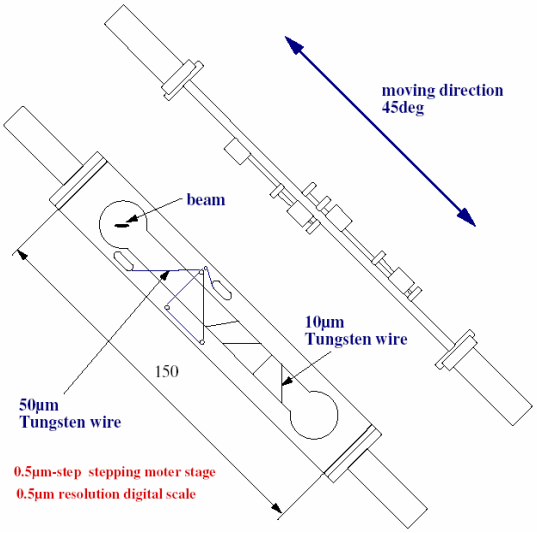

Fig. 40 Wire scanner mount from the ATF (courtesy H. Hayano, 2003).

The interaction of the beam with the wire may be detected in many ways: 1) by the change in voltage on the wire induced by secondary emission; 2) by detection of hard Bremsstrahlung whereby the forward detected photons are separated from the beam via an applied magnetic field (e.g. a normal bending dipole in a storage ring), converted to e+/e- pairs in the vacuum chamber wall, and detected with a Cerenkov counter or photomultiplier tube (PMT) after conversion back to photons in the front end of the detector; 3) via detection of delta-rays at 90º using Cerenkov counters or PMTs; 4) by detection of scattering and electromagnetic showers using PMTs; 5) and novelly, by the detection of the change in tension of the wire. Of the above methods, option 4 finds most widespread use in high energy accelerators. In this case, the amplitude of the PMT signal is recorded as a function of the calibrated position of the wire.

Particular concerns of wire scanners include the dynamic range of the detectors (trade-off between good signal-to-noise characteristics and possible saturation for high single-bunch beam currents), vibrations of the wire, single-pulse beam heating (the instantaneous temperature in the wire should not exceed the melting point of the wire material), the wire thickness which adds in quadrature with the measured beam size (and should therefore be small), and, particularly in

circular accelerators, higher-order modes introduced by the vacuum chamber geometry surrounding the wire and the wire itself.

The wire scanner assembly and an example beam size measurement from the ATF [40] are shown in Figs. 41 and 42. These measurements together with data from a laser wire located in the damping ring are used routinely in the demonstration of record small vertical beam emittances at the ATF.

Fig. 41 Wire scanner assembly in the extraction line of the ATF damping ring (courtesy H. Hayano, 2003).

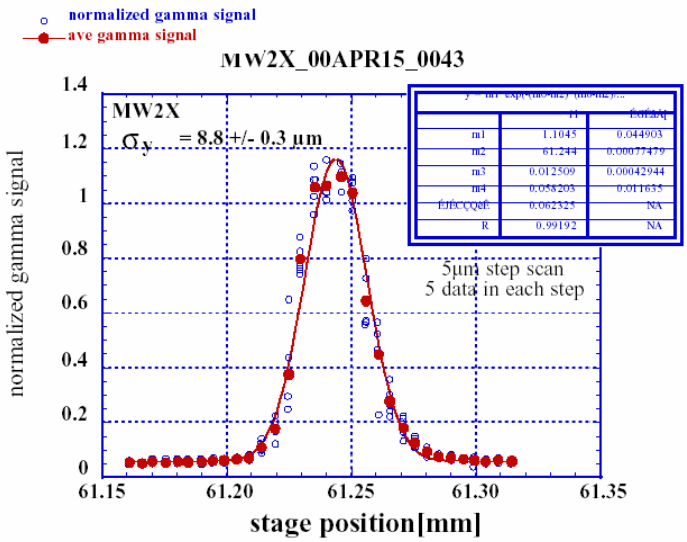

Fig. 42 Vertical beam size measured in the ATF extraction line using a wire scanner (courtesy H. Hayano, 2003).

5.3.4 Measurement of the transverse beam size using laser wires

At the expense of increased cost and complexity, the use of a laser as the interaction medium allows for a noninvasive measurement of the beam sizes. Moreover, as opposed to measurements with screens or conventional wires, the wire itself (in this case the laser) is (advantageously) non-destructable. A schematic of the laser wire system as installed [41] in PETRA at DESY and planned for use in PETRA-3, a third generation light source, is shown in Fig. 43. The system consists of a high-power laser, the optical transport line, the laser-lepton interaction region, and detectors. Measurement of the horizontal beam size is made using the optical path containing the deflector while the vertical beam size is measured using the optical path of the beam in the deflected arm of the beam splitter. The laser-beam interaction is detected using either the forward-scattered Compton photons or, after deflection by a magnetic field, the lower-energy scattered leptons of the particle beam.

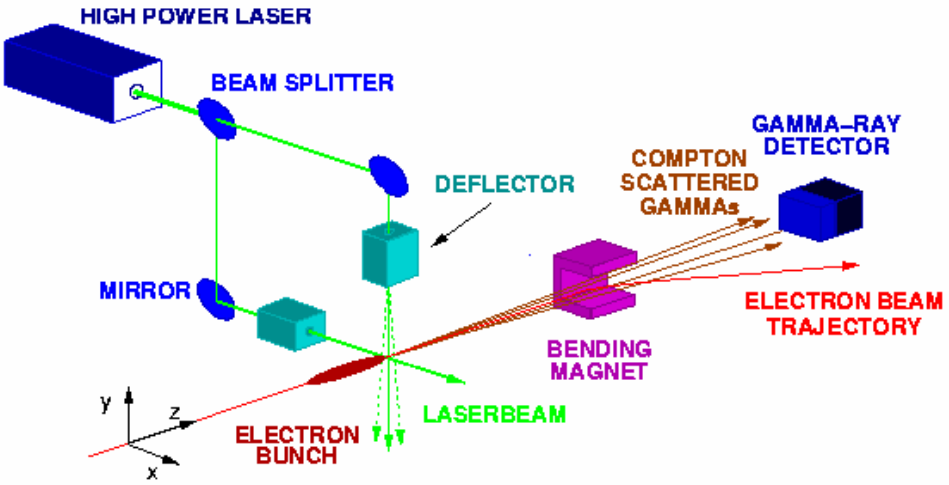

Fig. 43 Geometry of the laser-wire system for PETRA-3 at DESY (courtesy S. Schreiber, 2003).

A close-up view of the interaction region optics is shown in Fig. 44 from the pioneering laser wire experiment [42] performed in the SLC at SLAC. As with all applications of laser wires to date (at the SLC, the ATF, and at PETRA-3) experience has shown the following issues to be of importance: the size of the laser waist (in practice, the minimum waist size is on the order of the laser wavelength), background sources and background subtraction, the depth of focus, temporal synchronization of the laser with the beam (for the case of pulsed lasers), and, particularly for measurements of small beam sizes, accelerator reproducibility (which influences the time required to establish overlap of the laser with the beam).

In the laser wire facility in the ATF at KEK [43] the intensity of the laser is amplified using an optical cavity as shown in Fig. 45. Here the optical cavity is pumped by a CW laser with a mirror reflectivity exceeding 99%. A measurement of the vertical beam size in the ATF damping ring is shown in Fig. 46. As with normal wires, the wire size and additive contributions due to the vertical dispersion η_y (for the case of the vertical beam size measurement shown in Fig. 45) must be taken into account [43]. The correction for the wire size is

$$\sigma_y = \sqrt{{\sigma_{\rm obs}}^2 - (\frac{w_0}{2})^2} \tag{60}$$

where ω_0 is the 2σ wire thickness. The correction for the vertical dispersion is given, as usual, by

$$\beta_y \epsilon_y = (\sigma_y)^2 - (\eta_y \frac{\sigma_p}{p})^2 \tag{61}$$

where σ_p/p denotes the momentum spread of the particle beam. This state-of-the-art beam size measurement verified the exceedingly small design vertical emittance as required for a future linear collider.

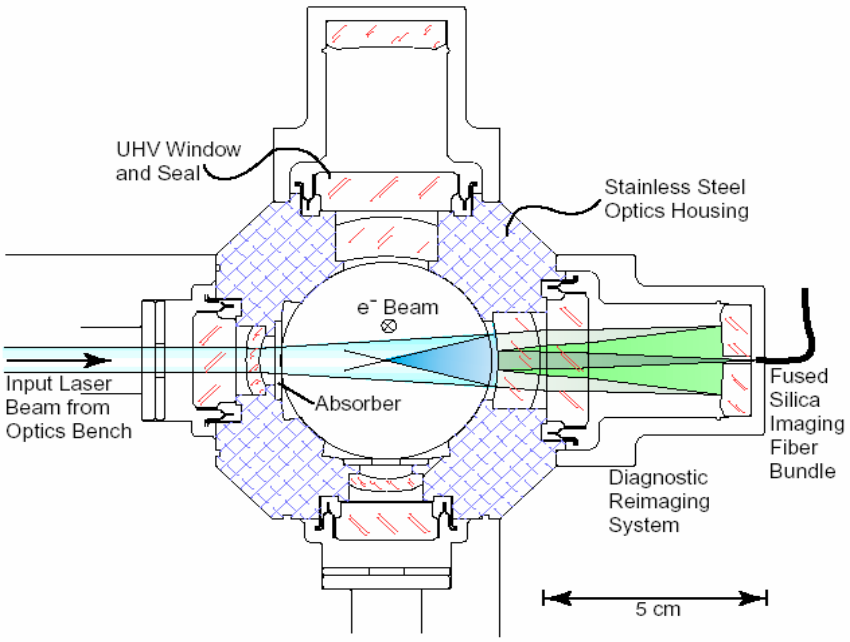

Fig. 44 Interaction region optics for the SLC laser wire (courtesy M. Ross, 2003).

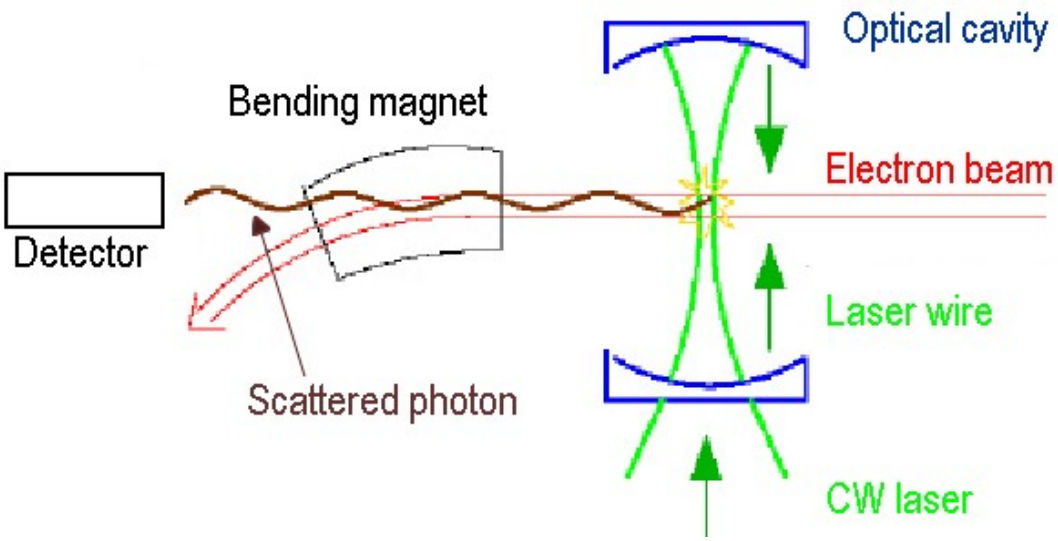

Fig. 45 Schematic of the laser wire at the ATF using an optical cavity (courtesy H. Sakai and J. Urakawa, 2003).

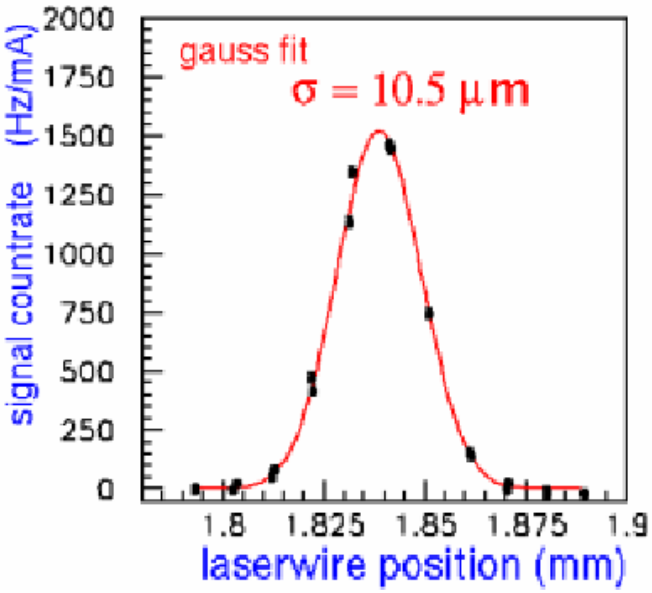

Fig. 46 Vertical beam size measurement from the ATF using a laser wire (courtesy H. Sakai and J. Urakawa, 2003).

5.3.5 Measurement of the transverse beam size using synchrotron radiation

In this section we describe one of many methods used for measuring properties of the lepton beam in a circular accelerator using synchrotron radiation. Not includes in this lecture, yet of great significance, are among others, measurements made using pin-hole cameras [44], interferometric methods [45], or measurements based on the angular distribution of the photon beam [46]. In the examples presented, it is attempted to discuss is some detail special concerns of measurements utilizing direct imaging and the variety of ways in which a single (relatively low-cost) experimental setup utilizing screens (in this case for the photon beam) can be used to gain information about the circulating lepton beam.

We recall from the lectures of A. Hoffmann [46], that measurement of the synchrotron radiation emitted by accelerated leptons can be categorized as direct imaging (for which the beam size is directly measured) or as direct observation (for which the angular spread of the beam is measured). These principles are illustrated schematically in Fig. 47. In the first case of direct imaging, the radiation emitted from a bending magnet is focused onto the detector using optical lenses. In the second case, the angular spread of the emitted radiation is observed directly.

Considering the first case, for which the radiation is emitted in a bending magnet, "depth of field" effects [47] must be taken into account. This refers to the fact that the photons are emitted continuously as they are bent (accelerated transversely) in the deflecting field of the magnet. The geometry is illustrated in Fig. 48 (top) from which can be seen that the photons are collected in the detector, located nominally to view the tangentially emitted radiation, not only from the ideal source emission point, but along the path of the lepton beam. The undesired contributions depend on the acceptance of the detector or on aperture restrictions given by the optical elements between the emission points and the detector. Viewed in the reference frame of the photon beam phase space, as shown in Fig. 48 (bottom), the particle beam emits a "swath" of radiation with a

curvature related to the curvature of the orbit. For example, referring to Fig. 48 (top), the beam emits radiation at +x for emission both before and after the nominal source-point emission location and has a point-source emission angle of +/- x'. The width of the "swath" is given by the transverse size of the lepton beam. Also shown in Fig. 48 (bottom) are the effects of limiting apertures (i.e. lens diameters or the camera acceptance). Here a is the half-width of the limiting aperture and l is the distance to this defining aperture.

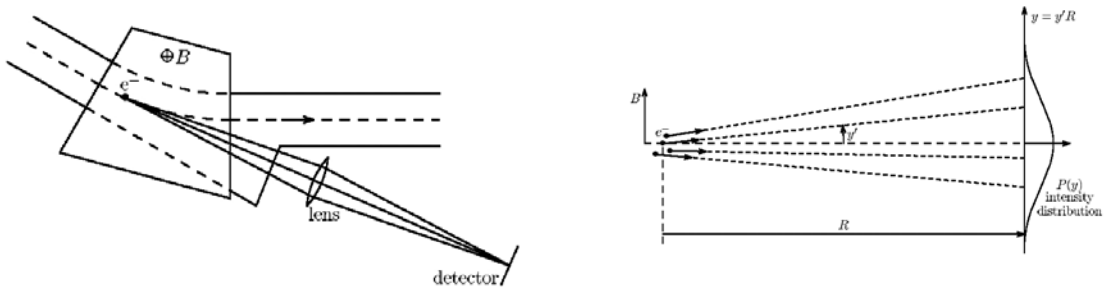

Fig. 47 Conceptual diagrams illustrating direct imaging (left) or direct observation of the angular spread of the emitted synchrotron radiation (right) for determination of the transverse beam size (courtesy A. Hoffmann, these lecture series, 2003).

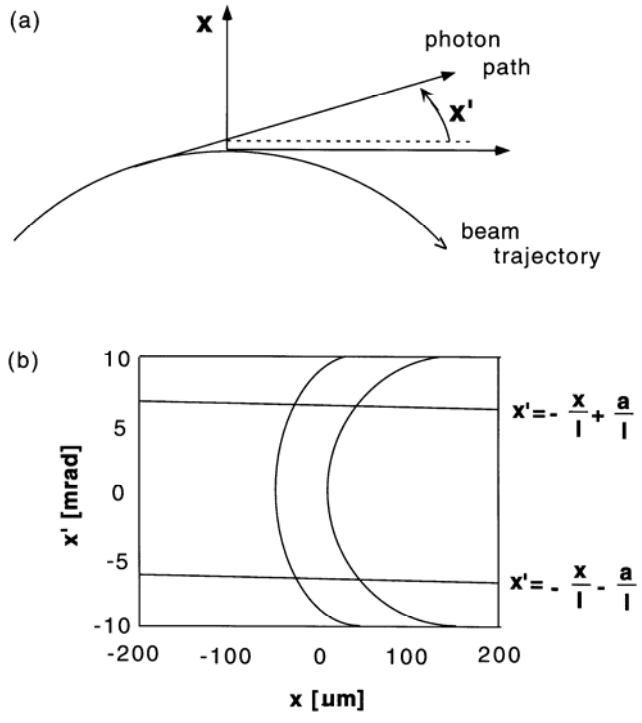

Fig. 48 Geometry of emitted synchrotron radiation in the horizontal plane illustrating contributions due to depth-of-field and the phase space coordinates of the photon beam (a) and the phase space of the photon beam assuming a bending radius of ρ=2 m, a beam size of σ=100 μm, and limiting apertures defined by the half-width a=1 cm and the distance to the aperture of l=1.46 m (b) [47,48].

The measured photon beam centroid <x> and beam size $\sigma_{r,x}$ correspond to a projection of the photon phase space (see Fig. 48b) onto the horizontal axis:

$$\bar{x} = \frac{\int I(x)x dx}{\int I(x)dx} \tag{62}$$

and

$$\sigma_{r,x}{}^2 = \frac{\int I(x)(x-\bar{x})^2 dx}{\int I(x)dx} \tag{63}$$

where I(x) denotes the intensity of the photon beam distribution. From Fig. 48 it is clear that depth-of-field effects may be minimized (at the cost of reduced light intensity) by reducing the size of the limiting aperture (the two parallel lines in Fig. 48b move closer together). With large apertures, the projection (and hence the measured image) would evidence a one-sided "tail" in the distribution and hence be non-Gaussian.

In the following is presented data taken in the SLC damping rings using direct imaging of synchrotron radiation. While the initial goal of the experiment was accurate determination of the transverse damping times [48], since these are perhaps not of foremost interest in the synchrotron radiation facility community, instead, the additional measurements of the beam emittance and matching at injection (which may be of concern in synchrotron light facilities to maximize injection efficiency) will be presented [49]. The layout of the optical system is shown in Fig. 49. In this case, the radiation was extracted from the vacuum chamber using a water-cooled Molybdenum mirror. The 1.33 m achromatic lens was used to produce parallel rays for transport to a remote location, which was necessary to avoid the high background radiation levels in the accelerator tunnel and was desired in order to have the camera accessible during normal operations. Special care was taken to avoid distortions of the beam image resulting from air currents generated between the (warm) tunnel and (cooler) room containing the optical table. At the remote location, the light was focused and then split using a pellicle. The image was viewed by two cameras, a "normal camera" for continuous monitoring of the beam and by a fast-gated camera used for turn-by-turn imaging of the lepton beam. The fast shutter was used to protect the delicate fast-gated camera from dangerous light levels when data were not being acquired. The polarized filters were used to filter out the contributions from the (bi-modal) transverse polarization of the photon beam. The location of the image focus was determined experimentally by translating the cameras along the optical path to obtain a minimum image size.

Shown in Fig. 50 is a close-up view of the camera apparatus. To remove scrolling (as seen on a camera "lines" that sweep vertically with time) resulting from electromagnetic interference the line-locked normal camera was used to supply composite synchronization to the gated camera. The video amplifier was used to boost the voltage level of the synchronized signal. The controller was used to adjust the gain and phase of the output video signal. A video digitizer clock interface (VDCI) and a transient wave form recorder (TWR) were used as in the previously existing automated emittance measurement systems at SLAC.

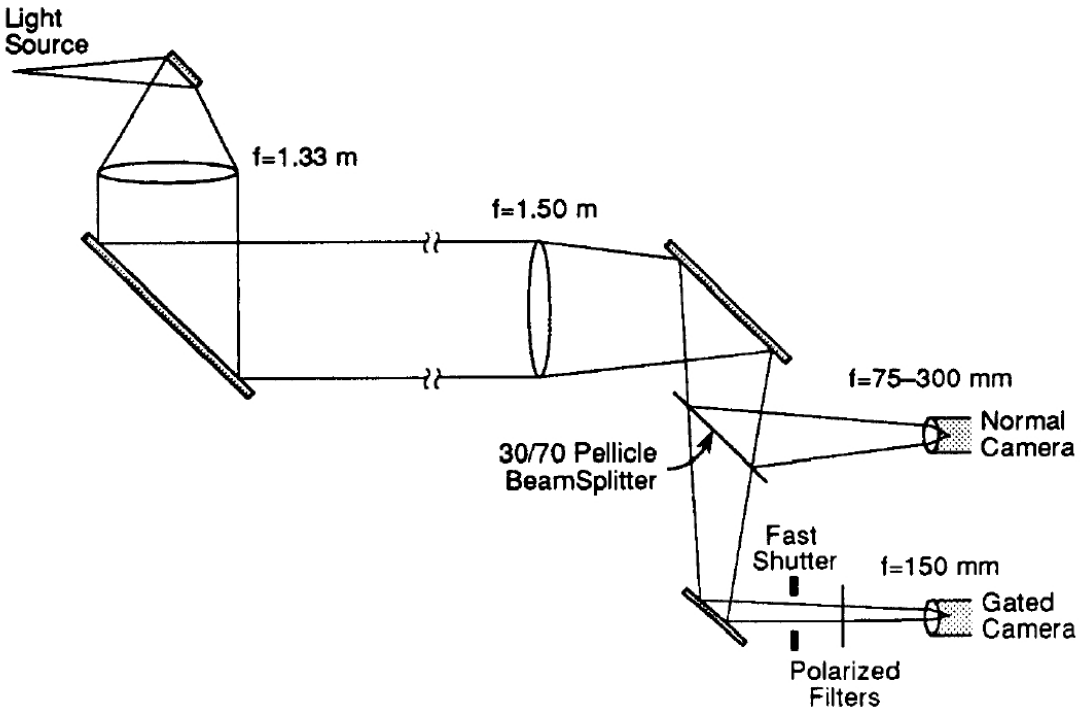

Fig. 49 Light optics used to produce parallel rays for transport to a remote location for direct imaging of the synchrotron radiation in the damping rings at the SLC. The overview is not to scale.

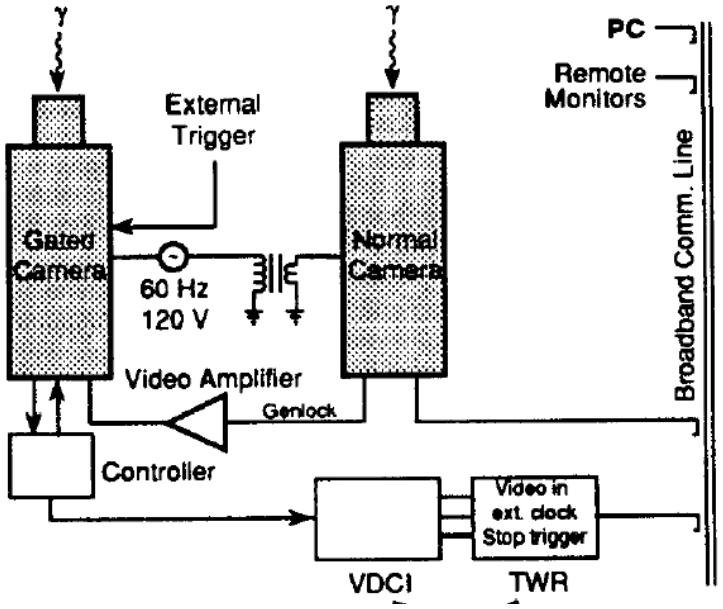

Fig. 50 Synchronization scheme using an additional "normal" camera.

In Fig. 51 is depicted the raw data showing turn-by-turn transverse beam profiles acquired at injection (with each image representing an average over 8 different beam pulses). The data were obtained by advancing the camera trigger by one revolution for each snapshot. A background image was subtracted from all snapshots and nearest-neighbor pixel averaging (smoothing) was performed to more clearly distinguish the intensity contours. As can be seen, the beam

distribution varied dramatically from turn-to-turn. After the beam filamented (after ~10 μs/100 ns = 100 turns), the beam image was seen to be elliptical with a Gaussian distribution. It is worth mentioning that the accelerator was operated on the coupling resonance with Qx~Qy=0.25 so that one might expect that every fourth turn result in an identical beam image (i.e. along every row). The differences in images along a given row may be partly attributable to amplitude-dependent tune shifts (arising from non-centered orbits in the sextupole magnets).

Quantitative information of the beam distribution was obtained, as in the case of transverse beam size measurements utilizing screens or wires, by digitizing the image, subtracting a background image, projecting the distributions along two normal axes, and fitting the results with a Gaussian distribution. An example is shown in Fig. 52.

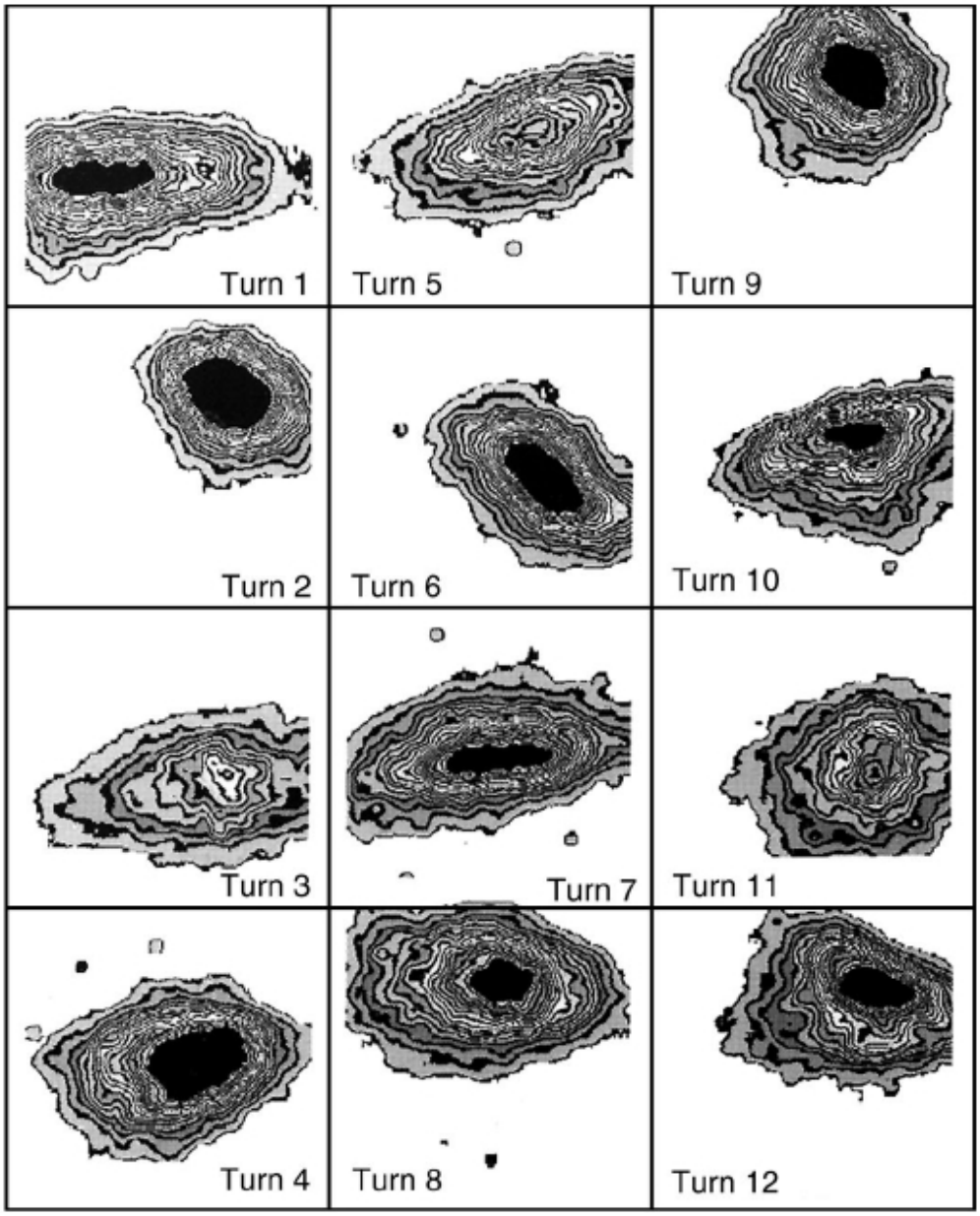

Fig. 51 Transverse beam profiles (in the x-y plane) using direct imaging as a function of turn number in the SLC damping ring.

As in the case of the wire scanner data presented previously one is confronted with the difficulty of qualitatively characterizing the measured profiles. As discussed previously one can apply a fit (either Gaussian or bi-Gaussian) and postulate that the fitted σ is fairly representative of the true rms of the distribution. While this parametrization is clearly not strictly true, it was found to be useful for further beam optimization. This is illustrated by the measurement results of Figs. 53 and 54. Plotted in both cases, on the left is the measured beam size squared (in the horizontal and vertical planes) measured turn-by-turn at injection. On the right are shown the Fourier transform of these data. In the case of perfect matching of the optical functions between the injection line and the downstream circular accelerator, the beam sizes would be constant from turn-to-turn. Given a mismatch peaks in the Fourier spectrum are discernible at frequencies of 2Q for a betatron mismatch (Δβ) and at Q for a dispersion mismatch (Δη) [49]. Figure 53 shows the measurement results before optimizing the injection match (evidencing prominent peaks due to the mismatches in β and η). The data obtained after correction are shown in Fig. 54. The optimization was performed empirically, using as a diagnostic the fitted beam size measured after the beam had fully filamented, by varying the strength of the quadrupoles at the end of the injection line.

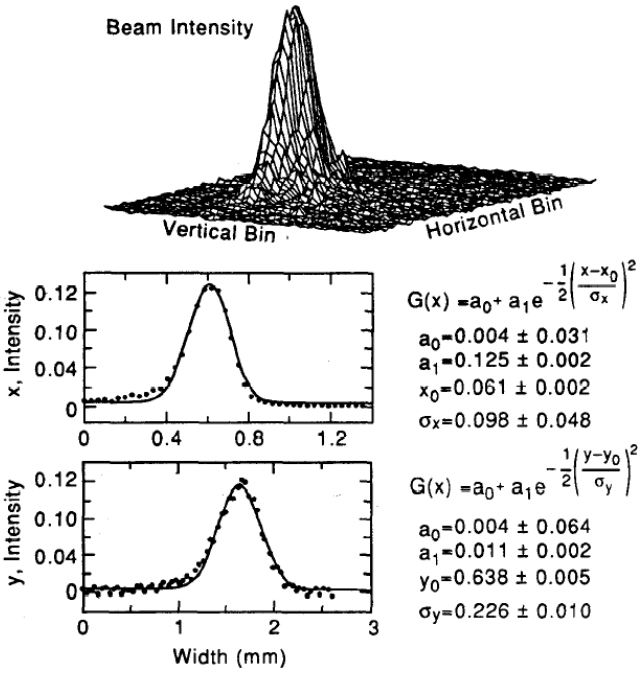

Fig. 52 Processed data from direct imaging. Shown is the 3-dimensional digitized image after background subtraction (top) and the projections together with the Gaussian fits (bottom).

The amplitude of the aberrant peaks gives qualitative information about the optical errors [49]. Considering for illustration purposes the case of a pure betatron mismatch, following the convention of M. Sands [29], the amplitude of the mismatch parameter B can be quantified. Denoting A_1 as the amplitude of the peak at zero frequency (dc) and A_2 the amplitude of the peak at twice the betatron frequency, it can be shown that $A_1=B\varepsilon_0$, where ε is the beam emittance in the plane of interest and $A_2=\varepsilon\bullet\text{sqrt}(B^2-1)$. Denoting the measured ratio of the amplitude of the peaks at dc and at twice the betatron frequency as ρ, the amplitude of the mismatch parameter can be solved for independent of knowledge of the β-function at the source emission point: $B=1/\text{sqrt}(1-\rho^{-2})$. For the case of complete filamentation without damping mechanisms, the beam emittance after the number of turns required for complete filamentation would be $\varepsilon=B\varepsilon_0$. If the β-function at the source emission point is known (or measured using, for example, a quadrupole

scan) and if the matching is perfect (B=1), then the amplitude of the DC component of the Fourier transform of σ^2 gives directly the beam emittance: $\sigma=\mathrm{sqrt}(A_1\beta)$.

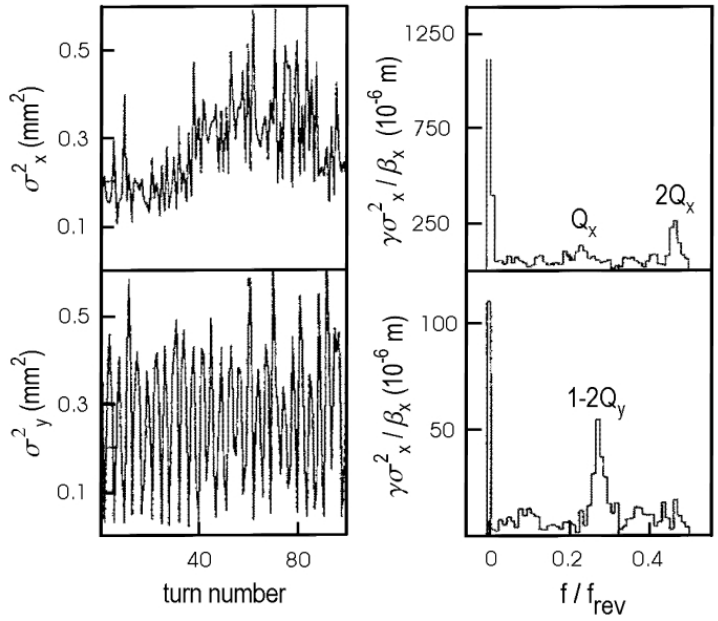

Fig. 53 Turn-by-turn measurement of the transverse beam sizes (left) and the Fourier spectrum of the beam shape oscillations (right) before injection matching.

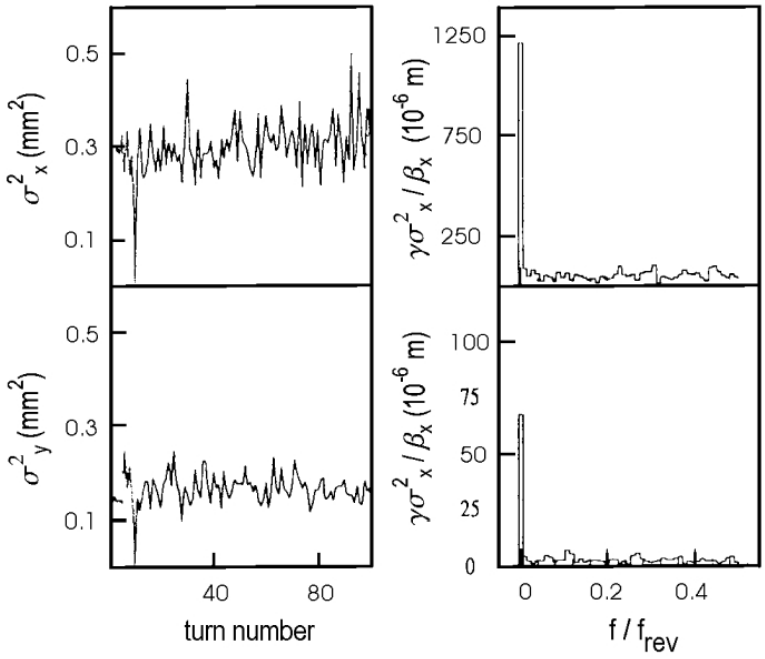

Fig. 54 Turn-by-turn measurement of the transverse beam sizes (left) and the Fourier spectrum of the beam shape oscillations (right) after injection matching.

6. MEASUREMENT OF THE BEAM ENERGY SPREAD USING SCREENS

In circular accelerators the beam energy spread is usually very small (~10^{-4}). The longitudinal acceptance determined mostly by the rf cavity voltage is usually large (since for leptons the energy losses due to synchrotron radiation are large and are compensated by large accelerating voltages) so energy spread measurements in synchrotron light facilities are not made often[11]. In linear accelerators with transfer lines however, a large single-bunch energy spread can lead to beam loss in the transfer lines (with non-zero dispersion) and, as in the case of the SLC, was seen to be important with respect to detector backgrounds since off-energy particles were differently focused near the interaction point. Shown schematically in Fig. 55 is the energy spread one would measure (right) in the case of long bunches (here "long" may be as small as 1/10th of the wavelength of the accelerating rf) in the limits of low and high single-bunch beam currents. In the low-current case (Fig. 55, top), a bunch placed near the crest of the accelerating rf (as desired for maximum acceleration) has a projection (right) evidencing a minimum energy spread. An off-crest acceleration, in the case of a low current bunch, would have a correspondingly larger energy spread. In the case of high single-bunch beam currents (Fig. 55, bottom), the on-crest bunch has a larger energy spread since the beam-induced voltage is not compensated for. In the high-current case, minimum energy spread is obtained by placing the beam off crest (e.g. changing the phase of the accelerating rf). In the illustration is shown optimal phasing for which the beam-induced voltage (dashed line) perfectly compensates the gradient in the accelerating rf.

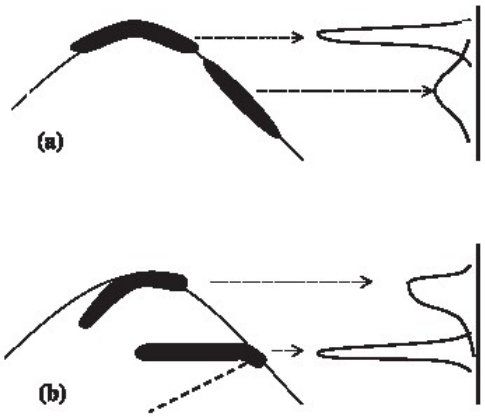

Fig. 55 Effective energy gain (left) and energy spread (right) for low (a) and high (b) single-bunch beam currents illustrating optimum phasing of the rf structures for minimum energy spread in a linear accelerator.

Measurement of the beam energy spread in a linear accelerator is quite straight-forward using a screen or a wire in a region of high dispersion (e.g. behind a bending magnet). The bending magnet generates dispersion η, which characterizes the fact that low-energy particles are more strongly deflected than high-energy particles, and so is a property of the magnetic lattice. The measured beam size is a convolution of the natural beam size σ_β and the contribution from the beam energy spread $\delta=\Delta E/E$:

$$\sigma = \sqrt{{\sigma_\beta}^2 + [\eta\delta]^2} \tag{64}$$

[11] The ability to measure the beam energy spread in the SLC damping rings, however, became critical as the single-bunch intensities were raised and a microwave instability in the damping ring became an issue for detector backgrounds 3 km away. The energy spread of the beam in this case was made downstream after changing the optics in the downstream transfer line to produce large dispersion at a screen.

By proper selection of location for the screen/wire behind the bending magnet, the dispersive contribution should be made to be large in comparison with the contribution from the natural beam size.

The layout of the TESLA Test Facility (TTF) is shown in Fig. 56. Measurements of the beam energy spread were made using an OTR screen at the end of the linac following the energy spectrometer. Single-bunch energy spreads as a function of the phase of the downstream accelerating module are shown in Fig. 57 measured with moderate single-bunch beam currents. Comparison with Fig. 55 shows good compensation of the beam-induced voltage at an rf phase angle of about +7º and poor phasing at an rf phase of -14º, for example. The substructure observed within a single bunch [50] has been attributed [51] to coherent synchrotron radiation generated in the bunch compressor, which was used nominally to compress the bunch length by about a factor of 4 (from 2 mm to 0.5 mm).

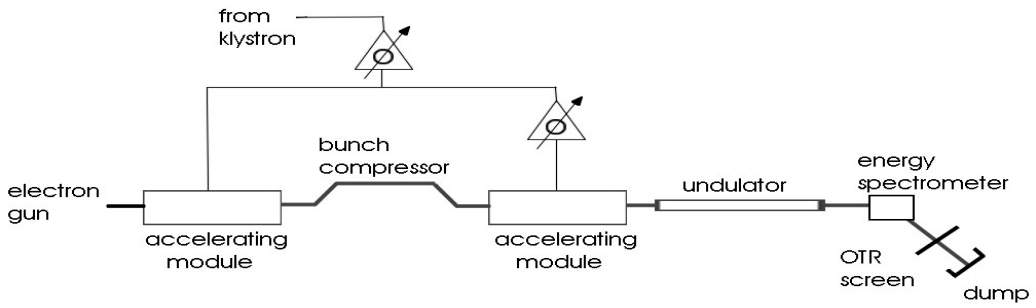

Fig. 56 Layout of the TESLA Test Facility (TTF-1).

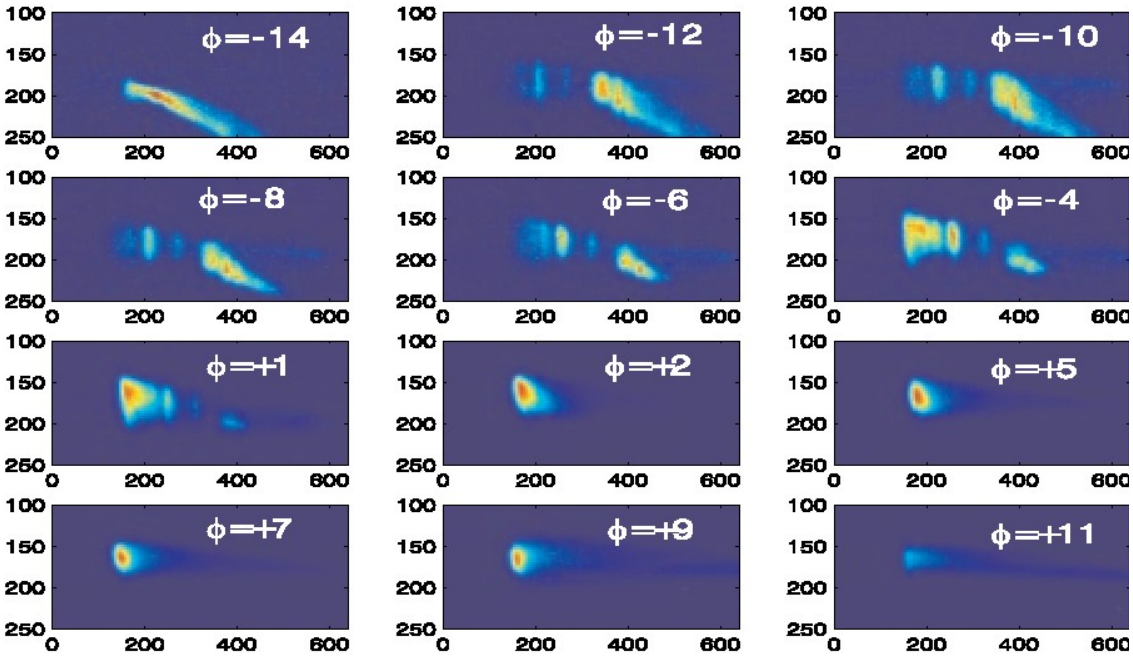

Fig. 57 Measurements of the single-bunch energy spread at the end of the TTF-1 linac (courtesy F. Stulle, 2003).

7. MEASUREMENT OF THE BUNCH LENGTH

The FEL community is challenged by resolution limitations for measurements of single-bunch bunch lengths. Recent theoretical analyses of the beam dynamics at the SASE FEL at the TESLA test facility have shown that only a small fraction (~50 fs) of the bunch contributed to the lasing process [52] and imply that all methods used to date (e.g. streak camera measurements, electro-optical sampling, interferometry, etc) were in this application resolution limited. While each and every R&D effort warrants further elaboration, since at the time of this writing the conclusions of these advanced efforts are still in flux, we opt to describe rather the conventional method of bunch length determination using streak cameras which is a primary tool for storage ring facilities.

7.1 Measurement of the bunch length using a streak camera

As shown in Fig. 58, photons (generated e.g. by synchrotron radiation, optical transition radiation, or from an FEL) after collimation and optics adjustment are converted into electrons in the photocathode of the streak camera. These electrons are accelerated by a biasing field and deflected using a time-synchronized, ramped electric field. In this way those particles within the bunch arriving latest (at the tail of the bunch) experience the highest deflection so that the temporal properties of the beam are visible in the transverse plane. The electron beam signal is sometimes further amplified using a multiple channel plate detector (MCP). The electrons are converted back into photons (via a phosphor screen) and detected using an imager (i.e. CCD array) which converts the light signal into a voltage.

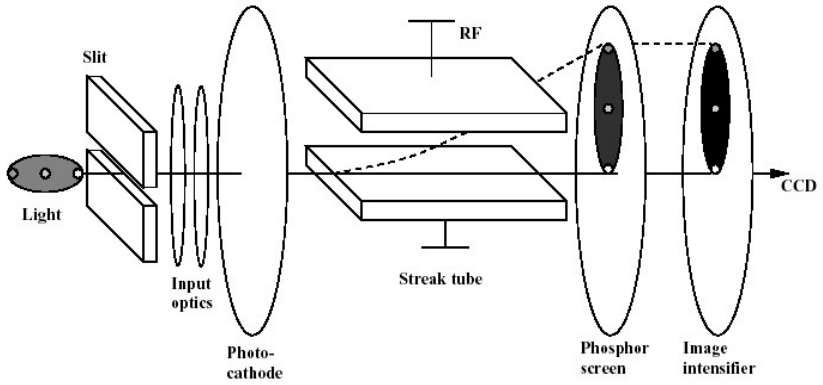

Fig. 58 Principle of a streak camera [53].

Practical issues that arise in streak camera measurements include the energy spread of the electrons from the photocathode (time dispersion), space charge effects immediately after the photocathode, and chromatic effects which change the particle arrival time in an energy-correlated way arising, for example, in the windows that separate the vacuum system from air.

Streak camera images taken at the Pohang light source are shown in Fig. 59. These data were acquired in study of fast-ion instabilities predicted [54] to arise in electron storage rings when ions in the residual gas are attracted resonantly to the passing bunches of an electron beam. In the figure, time decreases towards the bottom of each sub-plot (the most recent data are at the bottom of each plot). The horizontal axis is the temporal coordinate. Visible are the bunch lengths of six bunches (top left plot). As the residual gas pressure was intentionally increased, the bunches

were observed to begin to oscillate coherently in a manner consistent with that expected from the fast-ion instability [55].

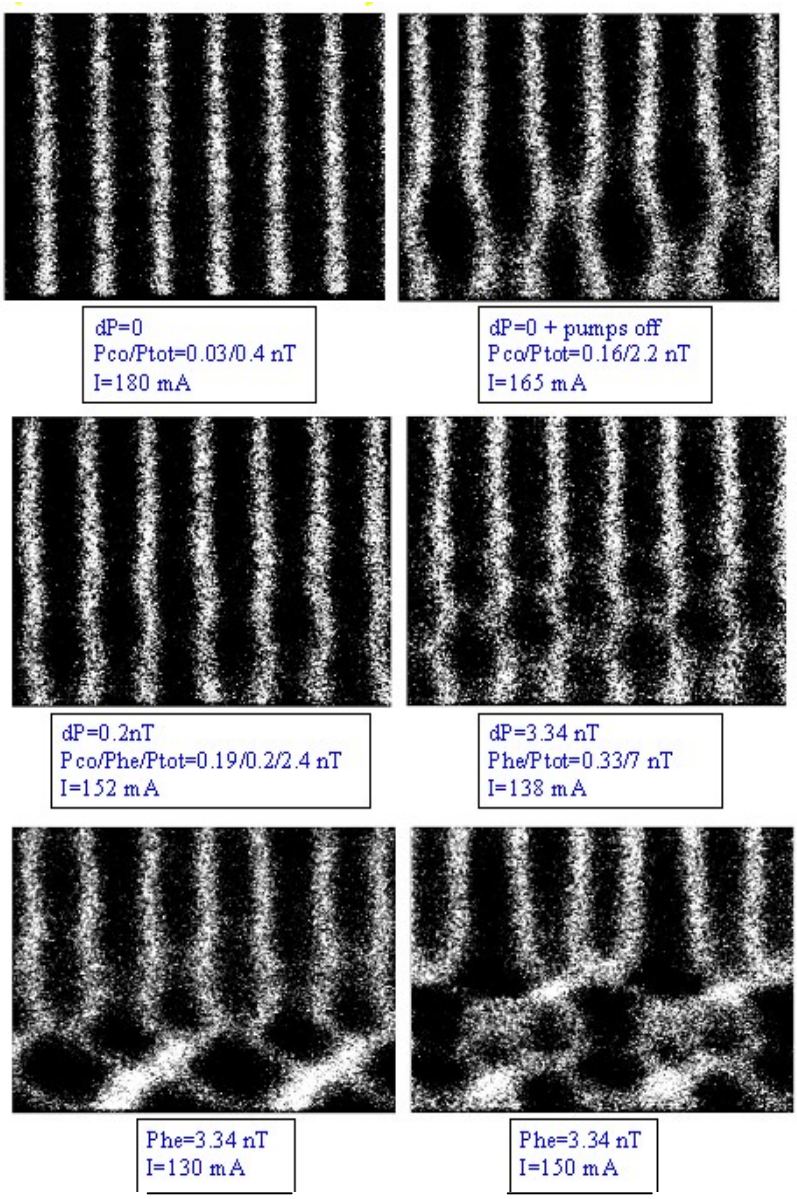

Fig. 59 Streak camera images from the Pohang light source evidencing beam oscillations arising from the fast-ion instability (courtesy M. Kwon, 2000).

7.2 Bunch length measurements using a transverse-mode deflecting cavity and screens

Based on a concept used at SLAC in 1965 [56], use of transverse-mode deflecting cavities has gained recent interest now applied to bunch length measurements in FEL facilities [57-59]. The deflecting cavity, which has a large TM_{11}-mode so that a bunch with a transverse displacement receives a large deflection, is used to "sweep" the beam (just like in the case of a streak camera),

which is then detected using standard profile monitors. The concept is illustrated schematically in Fig. 60.

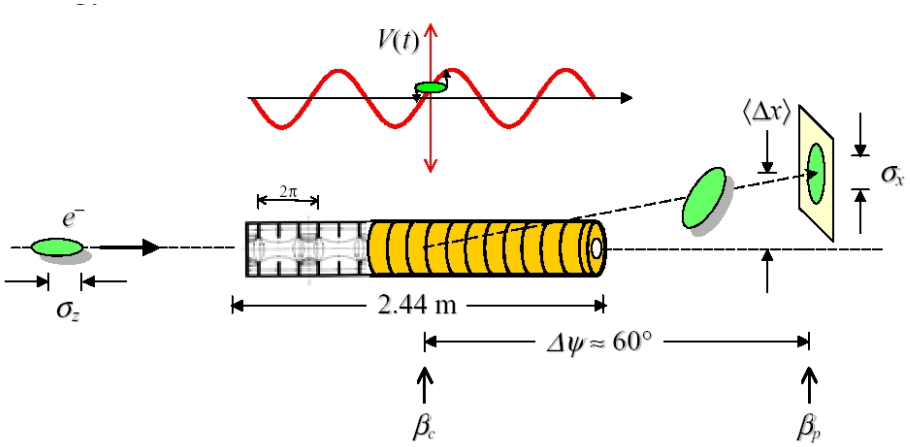

Fig. 60 Principle of the transverse mode cavity as installed and tested at SLAC (courtesy R. Akre, 2003).

The image detected on the screen is as usual projected and fitted with a Gaussian distribution (after background subtraction). Measurement of the bunch length, presented as the square of the measured bunch length versus applied voltage of the cavity are shown in Fig. 61. The deviation of the minimum bunch length measured from zero applied voltage has been attributed to evidence of an incoming tilt of the bunch [59].

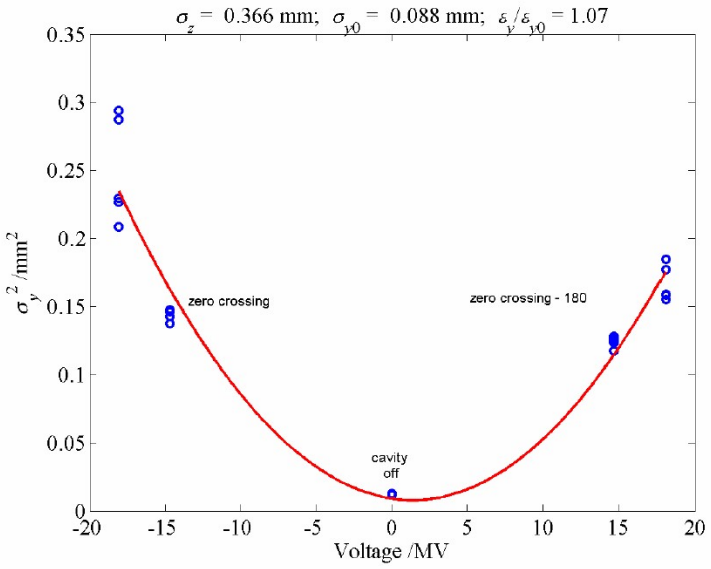

Fig. 61 Measured bunch length (squared) versus applied voltage in the transverse-mode deflecting cavity in measurements at SLAC (courtesy R. Akre, 2003).

8. SUMMARY

In these lectures were described the hardware applied for determining the most commonly measured moments of the beam distribution with focus on those devices used most frequently in synchrotron radiation and free electron laser facilities. In the first lecture, measurements of the zeroth and first order moments were discussed. Beam diagnostics were described as used for measuring the beam charge (using Faraday cups) and intensity (using toroidal transformers and BPM sum signals) and the beam position measured with wall gap monitors, electrostatic monitors (including buttons), stripline/transmission detectors, and resonant cavities. Equivalent circuit models were presented which were however often simplistic. In practice these models are often tailored to match observation given direct measurement or using computer models. Impedances in the electronics used to process the signals (which were not described) must also be taken into account as they often limit the bandwidth of the measurement. Nonetheless, the fundamental design features of the detectors presented were discussed thus highlighting the importance of detector geometries and impedance matching as required for high measurement sensitivity.

The second lecture focused on measurement of the second moments of the beam distribution. Multiple, equivalent methods for describing the transport of beam parameters between two points were reviewed. Two methods for measuring the transverse beam emittance were outlined in detail: the method of the quadrupole scan, an invasive measurement during which the accelerator optic (e.g. quadrupole field strength) is varied and measurements are made at a single location, and the fixed-optics method, which requires at least three independent beam size measurements and assumes that the optics between measurements is known. Experimental hardware applied in measurements of the beam size were reviewed including the use of screens, transition radiation, conventional and laser wire scanners, and direct imaging of synchrotron radiation. Measurements of the beam energy spread using screens and the bunch length using streak cameras and transvers-mode deflecting cavities were reviewed.

ACKNOWLEDGEMENTS

In preparation of these lectures, I have profitted enourmously from recent insightful conversations with M. Dohlus, K. Honkavaara, R. Neumann, D. Noelle, S. Schreiber, L. Schreiter, T. Shintake, M. Werner, and M. Wendt. For their enthusiasm, insights, and furthering of my education in the subject of beam diagnostics, I would like especially to thank W. Kriens, R. Pollock, M.C. Ross, and R.H. Siemann.

REFERENCES

[1] J. Borer and R. Jung, Diagnostics, CERN LEP-BI/84-14 (1984); CERN Accel. School on Antiprotons for Colliding Beam Facilities (Geneva, Switzerland, 1984) 385.

[2] R. Littauer, Beam instrumentation, Proc. Physics of High Energy Particle Accelerators (Stanford, CA, 1982); AIP Conf. Proc. 105 (1982) 869.

[3] A. Hofmann, Beam diagnostics and applications, Proc. Beam Instr. Wkshp. BIW98 (Stanford, CA, 1998); AIP Conf. Proc. 451 (1998) 3.

[4] R.H. Siemann, Bunched beam diagnostics, Proc. Physics of Part. Accel. (Batavia, IL, 1987) 430.

[5] R.H. Siemann, Spectral analysis of relativistic bunched beams, Proc. Beam Instr. Wkshp. BIW96 (Argonne, IL, 1996) 3.

[6] R. Talman, Beam current monitors, Proc. Acc. Instr. Wkshp. (Dallas, TX, 1989); AIP Conf. Proc. 212 (1989) 1.

[7] R.C. Webber, Tutorial on beam current monitoring, Proc. Beam Instr. Wkshp., BIW00 (Oak Ridge, TN, 2000); AIP Conf. Proc. 546 (2000).

[8] J.A. Hinkson, Beam current measurements, in Handbook of Accelerator Physics and Engineering, A.W. Chao and M. Tigner (eds.) (World Scientific, 1999).

[9] see for example the Particle Properties Data Booklet: L. Montanet et al., Phys. Rev. D50, 1173 (1994).

[10] T. Suwada, S. Ohsawa, K. Furukawa, N. Akasake, Absolute beam-charge measurement for single-bunch electron beams, Jpn. Jour. Appl. Phys. **39** (2000) 628.

[11] T. Suwada et al, Recalibration of a wall-current monitor using a Faraday cup for the KEKB injector linac, Proc. 1999 Part. Acc. Conf. (New York, NY,1999) 2238.

[12] Bergoz Precision Beam Instrumentation – www.bergoz.com

[13] K. Unser, Beam current transformer with DC to 200 MHz range, IEEE Trans. on Nucl. Sci., Vol. NS-16, No. 2 (1969).

[14] K. Unser, A toroidal dc current transformer with high resolution, IEEE Trans. on Nucl. Sci., Vol. NS-28, No. 3 (1981).

[15] J. Fusellier, J.M. Joly, Beam intensity monitoring and machine protection by toroidal transformers on the TESLA test facility, Proc. 5th Eur. Part. Acc. Conf. (Sitges, Spain, 1996) 1591.

[16] D. Boussard, Schottky noise and BTF diagnostics, CERN Accel. School on Advanced Accelerator Physics (Rhodes, Greece, 1993) 749.

[17] A.J. Gorski and R. M. Lill, Construction and measurment techniques for the APS LEUTL project rf beam position monitors, Proc. 1999 Part. Acc. Conf. (New York, NY,1999) 1411.

[18] R. Lorentz, Cavity beam position monitors, Proc. Beam Instr. Wkshp., BIW98 (Stanford, CA, 1998); AIP Conf. Proc. 451 (1998) 53.

[19] T. Shintake, Development of nanometer resolution RF-BPMs, given at the 17th Intl. Conf. on High-Energy Acc. HEACC98 (Dubna, Russia, 1998); KEK-preprint-98-1998.

[20] T. Slaton, G. Mazaheri, and T. Shintake, Development of nanometer resolution C band radio frequency beam position monitors in the final focus test beam, Proc. 19th Intl. Linear Acc. Conf., Linac98 (Chicago, IL,1998) 911.

[21] C. Magne and M. Wendt, Beam position monitors for the TESLA accelerator complex, DESY-TESLA-2000-41 (2000).

[22] Alternatively the undesired common-mode may be damped by clever design of the BPM. See, for example, S.C. Hartman, T. Shintake, and N. Akasaka, Nanometer resolution BPM using damped slot resonator, Proc. 1995 Part. Acc. Conf. (Dallas, TX,1995) 2655.

[23] J. Arthur et al, Linac coherent light source (LCLS) conceptual design report, SLAC-R-593 (2002).

[24] R. Bossart, High precision beam position monintor using a re-entrant coaxial cavity, Proc. 17th Intl. Linear Acc. Conf., Linac94 (Tsukuba, Japan,1994) 851.

[25] C. Magne et al, High resolution BPM for future colliders, Proc. 19th Intl. Linear Acc. Conf., Linac98 (Chicago, IL,1998) 323.

[26] M.C. Ross et al, Automated emittance measurements at the SLC, Proc. 1987 Part. Acc. Conf. (Washington, D.C., 1987) 725.

[27] H. Wiedemann, Particle accelerators physics: basic principles and linear beam dynamics (Springer Verlag, Berlin 1993).

[28] M. Minty and F. Zimmermann, Measurement and control of charged particle beams, (Springer Verlag, Berlin 2003).

[29] M. Sands, A beta mismatch parameter, SLAC-AP-085 (1991).

[30] P. Tenenbaum and T. Shintake, Measurement of small electron beam spots, Ann. Rev. Nucl. Part. Sci. **49** (1999) 125.

[31] R. Jung, G. Ferioli, S. Hutchins, Single pass optical profile monitoring, 6th Eur. Wkshp. on Beam Diagnostics and Instr. for Part. Acc., DIPAC2003 (Mainz, Germany, 2003).

[32] F.-J. Decker, R. Brown, and J.T. Seeman, Beam size measurements with noninterceptive off-axis screens, Proc. 1993 Part. Acc. Conf. (Washington, DC, 1993) 2507.

[33] J. Bosser et al, Optical transition radiation proton beam profile monitor, Nucl. Instrum. Meth. **A238** (1985) 45.

[34] D.W. Rule and R.B. Fiorito, Beam profiling with optical transition radiation, Proc. 1993 Part. Acc. Conf. (Washington, DC, 1993) 2453.

[35] R. Jung, G. Ferioli, and S. Hutchins, Single pass optical profile monitoring, Proc. DIPAC 2003 (Mainz, Germany, 2003)

[36] K. Honkavaara, New beam diagnostics at TTF, Proc. DESY Beschleuniger-Betriebsseminar (Grömitz, Germany, 2000); DESY M 00-05 (2000) 110.

[37] M. Ross et al, A very high resolution optical transition radiation beam profile monitor, Proc. Beam Instr. Wkshp. BIW02 (Upton, NY, 2002); AIP Conf. Proc. 648 (2003) 237.

[38] M.C. Ross, Wire scanner systems for beam size and emittance measurements at the SLC, Proc. of Acc. Instr. Conf. (Batavia, IL, 1990) 88.

[39] M.C. Ross et al, Wire scanners for beam size and emittance measurements at the SLC, Proc. 1991 Part. Acc. Conf. (San Fransisco, CA, 1991) 1201.

[40] H. Hayano, Wire scanners for small emittance beam measurements in ATF, Proc. 20th Intl. Linac Conf, Linac 2000; eConf C000821:MOc01,2000 (Monterey, CA, 2000) 146.

[41] T. Kamps et al, R&D towards a laser based beam size monitor for the future linear collider, Proc. 8th Eur. Part. Acc. Conf. (Paris, France, 2002) 1912.

[42] R. Alley et al, A laser based beam profile monitor for the SLC/SLD interaction region, Nucl. Instrum. Meth. **A379** (1996) 363.

[43] H. Sakai et al, Measurement of a small vertical emittance with a laser wire beam profile monitor, Phys. Rev. ST Accel. Beams **5**:122801 (2002).

[44] see for example J. Safranek and P.M. Stefan, Emittance measurement at the NSLS X-Ray Ring, Proc. 5th Eur. Part. Acc. Conf. (Sitges, Spain, 1996) 1573 ; C. Limborg et al, A pinhole camera for SPEAR 2, Proc. 7th Eur. Part. Acc. Conf. (Vienna, Austria, 2000) 1774.

[45] see for example T. Mitsuhashi and T. Naito, Measurement of beam size at the ATF damping ring with the sr interferometer, Proc. 6th Eur. Part. Acc. Conf. (Stockholm, Sweden, 1998) 1565 ; T. Shintake et al, Experiments of nanometer spot size monitor at FFTB using laser interferometry, Proc. 1995 Part. Acc. Conf., PAC95 (Dallas, TX, 1995) 2444.

[46] A. Hofmann (in this lecture series), Beam diagnostics with synchrotron radiation, to be published in Proc. CERN Accel. School on Synchrotron Radiation and Free-Electron Lasers (Brunnen, Switzerland, 2003).

[47] A.P. Sabersky, The geometry and optics of synchrotron radiation, Part. Accel. **5** (1973) 199; SLAC-PUB-1245 (1973).

[48] M. Minty et al, Using a fast gated camera for measurements of the transverse beam distributions and damping times, Proc. 1992 Acc. Instr. Wkshp. (Berkeley, CA, 1992) 158.

[49] M. Minty and W.Spence, Injection envelope matching in storage rings, Proc. 1995 Part. Acc. Conf. and Intl. Conf. on High Energy Accel (Dallas, TX, 1995) 536.

[50] M. Huening et al, Observation of longitudinal phase space fragmentation at the TESLA test facility free electron laser, Nucl. Instrum. Meth. **A475** (2001) 348.

[51] T. Limberg et al, An analysis of longitudinal phase space fragmentation at the TESLA test facility, Nucl. Instrum. Meth. **A475** (2001) 353.

[52] V. Ayvazian et al, Generation of GW radiation from a VUV free electron laser operating in the femtosecond regime, Phys. Rev. Lett. **88**:104802 (2002).

[53] M. Geitz, Bunch length measurements, Proc. DIPAC99 (Daresbury Laboratory, UK, 1999) 18.

[54] T.O. Raubenheimer and F. Zimmermann, Phys. Rev. E **52** (1995) 5487.

[55] J.Y. Huang et al, Study of the fast beam-ion instability in the Pohang light source, Proc. 6th Eur. Part. Acc. Conf. (Stockholm, Sweden, 1998) 276.

[56] G.A. Loew and O.H. Altenmueller, Design and application of rf deflecting structures at SLAC, PUB-135 (1965); R.H. Miller et al, The SLAC injector, IEEE Trans. Nucl. Sci. (1965) 804.

[57] X.-J. Wang, Producing and measuring small electron bunches, Proc. 1999 Part. Acc. Conf. (New York, NY, 1999) 229.

[58] R. Akre et al, A transverse RF deflecting structure for bunch length and phase space diagnostics, Proc. 2001 Part. Acc. Conf. (Chicago, IL, 2001) 2353.

[58] R. Akre et al, Bunch length measurements using a transverse rf deflecting structure in the SLAC linac, Proc. 8th Eur. Part. Acc. Conf. (Paris, France, 2002) 1882.